Crystallography of Fatigue Crack Initiation and Growth in Fully Lamellar Ti-6Al-4V

A.L. PILCHAK, R.E.A. WILLIAMS, and J.C. WILLIAMS

Fatigue crack initiation in titanium alloys is typically accompanied by the formation of planar, faceted features on the fracture surface. In the present study, quantitative tilt fractography, electron backscatter diffraction (EBSD), and the focused ion beam (FIB) have been used to provide a direct link between facet topography and the underlying microstructure, including the crystallographic orientation. In contrast to previous studies, which have focused mainly on the α-phase crystal orientation and the spatial orientation of the facets, the present analysis concentrates on the features that lie in the plane of the facet and how they relate to the underlying constituent phases and their crystallographic orientations. In addition, due to the anisotropic deformation behavior of the three basal slip systems, the orientation of the β phase as it relates to facet crystallography was investigated for the first time. The implication of the β-phase orientation on fatigue crack initiation was discussed in terms of its effect on slip behavior in lamellar microstructures. The effect of the local crystallographic orientation on fatigue crack initiation was also investigated by studying cracks that initiated naturally in the earliest stages of growth, which were revealed by FIB milling. The results indicate that boundaries that are crystallographically suited for slip transfer tend to initiate fatigue cracks. Several observations on the effect of the crystallographic orientation on the propagation of long fatigue cracks were also reported.

I. INTRODUCTION

THE union of electron backscatter diffraction (EBSD) and quantitative tilt fractography[1–3] has provided an efficient method for relating crystallographic information obtained directly from a fracture surface (or a polished face that intersects it) to the spatial orientation of features on it. The direct method, in which EBSD patterns are collected directly from the as-fractured surface without additional preparation, has been reported to have an accuracy between 1[3] and 3 deg[4] when the spatial information and crystallographic information are obtained in the same microscope session without rotating the stage. This method is limited, however, by the necessity for a relatively flat fractured surface that was not accompanied by substantial plasticity during fracture. Thus, this method is often used to study cleavage facets[5] in steels or fatigue facets[2,3,6–8] in titanium alloys. The formation of facets in titanium alloys is of particular interest, because the crack initiation stage has a dominant contribution to total

A.L. PILCHAK, formerly Graduate Research Associate, Department of Materials Science and Engineering, The Ohio State University, is currently Visiting Scientist, Air Force Research Laboratory, Materials and Manufacturing Directorate, Wright Patterson Air Force Base, OH 45433 and Research Scientist, Universal Technology Corporation, Dayton, OH 45432. Contact e-mail: pilchak@matscen-g.ohio-state.edu R.E.A. WILLIAMS, Graduate Research Associate, and J.C. WILLIAMS, Professor and Honda Chair, are with the Department of Materials Science and Engineering, The Ohio State University, Columbus, OH 43210.
Manuscript submitted June 5, 2009.
Article published online November 5, 2009

life during high-cycle fatigue loading. In addition, crack initiation during tests that include a dwell period is paramount to explaining the substantial reduction in life that accompanies this type of fatigue failure.[9] Previous studies have identified these facets as being parallel or nearly parallel to the basal plane.[2,3,6–8,10,11] The "near-basal" orientations can be accounted for by the presence of steps, which are similar to river markings, on the facet surface.[12] A complete description of facets, however, also requires reporting the spatial orientation of the facet in addition to the crystallographic plane of fracture.[2,3] For example, dwell facets are most frequently oriented nearly perpendicular to the applied loading direction in an orientation that has low resolved shear stress on the basal plane, but high resolved normal stress. In contrast, facets formed during continuous cycling often form in grains the basal planes of which are more highly inclined to the loading direction.[12–14] While these experimental works have identified the role of the α-phase crystallographic orientation in crack initiation in titanium alloys, the β-phase orientation has not been given any attention despite its significant effect on the mechanical behavior of materials containing lamellar constituents.[15–19]

In the present study, we extend the analysis of facet crystallography by introducing a method to determine the β-phase orientation. In addition to identifying the spatial and crystallographic orientation of the fracture facets, this study also focuses on the microscopic features that lie in the plane of the facets and how they relate to the underlying microstructural constituents. The results provide additional insight into the

micromechanisms associated with crack initiation and the early stages of faceted growth[12] in fully lamellar microstructures.

II. BACKGROUND

The majority of the following work relies on expressing the features on a fracture surface as points in a Cartesian coordinate system. This can be accomplished quickly and efficiently using quantitative tilt fractography. The technique has been described in detail in the literature,[1,3,20] but it is covered briefly in this section due to its extensive use in the present study. This is followed by a brief summary of the important aspects of the Burgers orientation relationship related to this work.

A. *Quantitative Tilt Fractography*

In the method described by Sinha *et al.*,[2,3] high-resolution secondary electron images of the same area are acquired at two different stage tilt angles using the same magnification. A common origin and three features (A, B, and C) that are recognizable in both images are identified. Next, the (x,y) coordinate of each feature with respect to the origin is determined and, using the geometrical relationships derived by Themelis *et al.*,[20] the (x,y) coordinate of each feature can be translated into the global sample reference frame defined by X-Y-Z.

$$X^i = \frac{x_1^i \cdot \sin \theta_2 - x_2^i \cdot \sin \theta_1}{\sin(\theta_2 - \theta_1)} \quad [1]$$

$$Y^i = y_1^i = y_2^i = \frac{y_1^i + y_2^i}{2} \quad [2]$$

$$Z^i = \frac{-x_1^i \cdot \cos \theta_2 + x_2^i \cdot \cos \theta_1}{\sin(\theta_2 - \theta_1)} \quad [3]$$

In Eqs. [1] through [3], (x_1^i, y_1^i) and (x_2^i, y_2^i) are the coordinates of the feature i at tilt angles of θ_1 and θ_2, respectively. Mapping two points from the fracture surface into the sample reference frame allows a vector to be constructed. For example, the vector connecting points A and B is determined by

$$\mathbf{AB} = (X^B - X^A)\mathbf{i} + (Y^B - Y^A)\mathbf{j} + (Z^B - Z^A)\mathbf{k} \quad [4]$$

Mapping a third point, C, into the sample reference allows a second vector $\mathbf{BC}$ to be defined and, thus, a plane can be defined. It is usually convenient to define the plane by its normal vector $\hat{\mathbf{n}}$:

$$\hat{\mathbf{n}} = \mathbf{AB} \times \mathbf{BC} \quad [5]$$

Any reference frame can be chosen as long as it is clearly defined and is self-consistent with the EBSD reference frame. In this study, the sample reference frame is related to the images taken in the microscopes, as shown in Figure 1. At 0 deg of stage tilt,
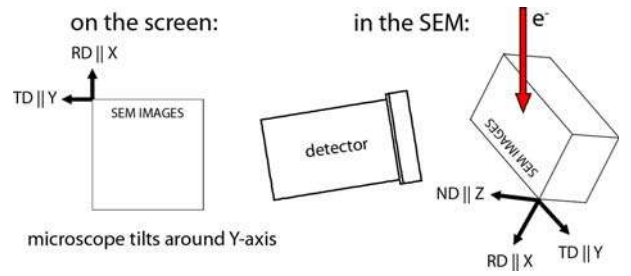

Fig. 1—Schematic representation of the sample reference frame used in this investigation.

the X-axis points up, the Y-axis points to the left, and the Z-axis points out of the plane of the image, which creates a right-handed orthonormal reference frame. In our experiments, the microscope stage tilts about the Y-axis. This reference frame is equivalent to the one utilized by the EBSD acquisition system in the microscope, which is defined by the RD-TD-ND coordinate system. After EBSD data have been collected, inverse pole figures are used to link the crystallographic orientation and spatial orientation. Inverse pole figures identify the $\{hkil\}$ perpendicular to a particular direction (vector) in the sample reference frame. However, the direction normal to the plane can be considered with the relationship:

$$\left\langle h\, k\, i\, \frac{3}{2}\left(\frac{c}{a}\right)^2 \right\rangle \quad [6]$$

where a and c are the lattice parameters of the alloy.

B. *Burgers Orientation Relationship and Parallelism of Slip Systems*

Burgers[21] identified the orientation relationship for the solid-state bcc (β) to hcp (α) phase transformation as being $(0001)_\alpha||(110)_\beta$ and $\langle 2\bar{1}\bar{1}0 \rangle_\alpha||\langle 1\bar{1}1 \rangle_\beta$. A schematic of the orientation relationship viewed from $[0001]_\alpha$ is shown in Figure 2. Because the $\langle a \rangle$ directions in the basal plane are 60 deg apart and the $\langle 111 \rangle_\beta$ directions in a given $\{110\}_\beta$ plane are 70.5 deg apart, only one $(0001)\langle 2\bar{1}\bar{1}0 \rangle$ slip system can be exactly parallel to a $\{110\}\langle 111 \rangle\beta$-phase slip system. This is referred to as the $\langle a_1 \rangle$ slip system in the literature[17–19,22] and it lies ~14.4 deg from the macroscopic α/β interface. The Burgers vectors on the other $\langle 111 \rangle_\beta$-phase slip system is rotated approximately 10.5 deg from its nearest α-phase slip system ($\langle a_2 \rangle$) and the third basal slip system ($\langle a_3 \rangle$) has no closely oriented $\{110\}\langle 111 \rangle\beta$-phase slip system. Although both phases have unique crystal structures and must deform independently, the parallelism of slip systems permits dislocations gliding on any of the three basal slip systems to pass through α/β interfaces. The dislocation reactions necessary for slip transfer across the interface have been studied with transmission electron microscopy (TEM) and were reported by Suri *et al.*[17] and Savage *et al.*[18,23,24] The difference in the required dislocation reactions for slip transfer among each basal slip system gives rise to

a_2 = $[\bar{1}\bar{1}20]$

$[\bar{2}110]$ // $[\bar{1}11\bar{1}]$

$[\bar{3}5\bar{3}]$

b_2 = $[\bar{1}11]$

~10.5°

$[1\bar{2}10]$

a_3 = $[\bar{1}2\bar{1}0]$

$[1\bar{1}\bar{1}]$ $[11\bar{2}0]$

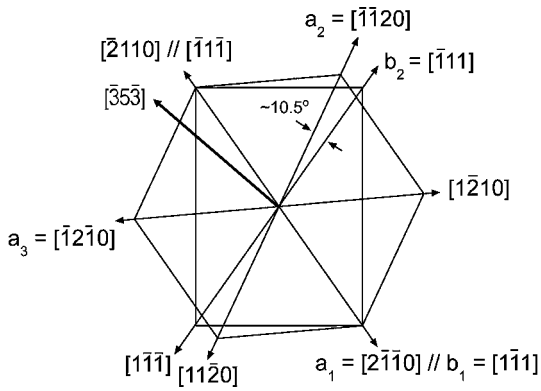a_1 = $[2\bar{1}\bar{1}0]$ // b_1 = $[1\bar{1}1]$

Fig. 2—Schematic representation of one of the 12 variants of the Burgers orientation relationship showing the relationship among the important slip directions in each phase. The $(0001)_\alpha$ and $(110)_\beta$ planes are parallel to the plane of the page, while the macroscopic α/β interface (lattice-invariant line) is located approximately 14.4 deg from the $\langle a_1 \rangle$ direction and is parallel to $[\bar{3}35]_\beta$.

unique yield stresses and work-hardening rates. Single-colony tension tests conducted on a near-α titanium alloy[18,23,24] have shown that the critical resolved shear stress (CRSS) and yield stress for basal slip increases in the order $\langle a_1 \rangle$, $\langle a_2 \rangle$, and $\langle a_3 \rangle$.

During the allotropic $\beta \rightarrow \alpha$ transformation, 12 distinct α variants can be inherited from a single parent β-grain orientation; however, due to symmetry, only 5 unique misorientations exist among any 2 adjacent colonies.[25] One unique pair of variants shares a common basal plane but has different $\langle 111 \rangle$ directions within that plane to satisfy the orientation relationship. While crystal symmetry dictates that this is only a 10.5-deg misorientation about [0001], the orientation relationship dictates that the lowest-energy interfaces, or broad faces,[22,26] will have angles on the order of approximately 80 deg between them.[26,27] Coincidence of the basal planes among two colonies does not necessarily ensure that the local slip length will be increased. Slip in each colony is a separate event and dislocation motion in one colony does not guarantee slip will occur in the second colony. This is due to the difference in the spatial orientations of the α/β interfaces, which can significantly affect the slip behavior of individual colonies.[15,16] This phenomenon has been addressed theoretically for single colonies by Chan[19] and experimentally by Pilchak[14] for fully lamellar Ti-6Al-4V under cyclic fatigue loading. This special combination of variants is important, however, because it is commonly observed at the catastrophic fatigue crack initiation sites of investment-cast Ti-6Al-4V.[12–14,28,29] As discussed later, this is related to the decreased small crack growth resistance for this specific pair of variants compared to the other high-angle boundaries.

III. EXPERIMENTAL PROCEDURES

A. Materials

The specimens analyzed in the present work were part of a study on the effect of yttrium (Y) on the high-cycle fatigue behavior of investment-cast and hot isostatically pressed Ti-6Al-4V.[30] The material was manufactured by doping a commercial Ti-6Al-4V melt with 200-ppm high-purity elemental Y. A cylindrical ingot was investment cast from the Y-doped melt. During cooling, the Y combined with oxygen and sulfur during cooling and precipitated as a submicron-sized oxysulfide particle. The particles had no effect on the microstructure of the alloy, which was typical of investment-cast Ti-6Al-4V consisting of coarse, fully lamellar $\alpha + \beta$ colonies that were contained within prior β grains that reached greater than 1 mm in diameter. In addition to 200-ppm Y, the alloy contained 6.34Al, 4.08V, 0.24Fe, and 0.19O by weight percent. In the study, five fatigue tests were performed by an independent laboratory at a maximum stress of 550 MPa with a load ratio $(\sigma_{min}/\sigma_{max})$ of 0.1 at a frequency of 50 Hz on the cast material. The fatigue specimens had smooth surfaces and were prepared by mechanical polishing in a self-consistent manner and tested according to ASTM E466 by an independent laboratory. Four of the specimens exhibited near-surface crack initiation, meaning that some portion of the first grain to crack bordered the free surface of the sample, while the longest-life specimen initiated on a completely subsurface facet. The term "near-surface" is used because, as shown later, the slip direction did not intersect the surface of the sample, so initiation was not caused by the classical slip band intrusion/extrusion mechanism.[31] It is noted that the near-surface initiation is not believed to be caused by residual stresses induced during sample preparation, driving initiation away from the surface. In fact, slightly subsurface initiation at α-grain or α-colony boundaries has been observed during four-point bending fatigue testing despite the stress being somewhat reduced below the surface.[13,14] If fatigue crack initiation were to occur by this mechanism in titanium alloys, it would be expected in the coarse, fully lamellar condition of the present study, especially with the high O content, which tends to deform by highly planar slip.[14] Excluding the subsurface initiation site, which was not representative of the other fractures, there was a fairly wide scatter band among the remaining four samples extending from ~700,000 cycles to 4.3 million cycles. Careful fractographic investigation showed that the fine-scale particles were not involved in the crack initiation process and concluded that the scatter in fatigue life must be attributed to another source. Bache et al.[10] have shown that the orientation of the grain in which the fatal crack initiates can be a dominant factor governing fatigue life. However, a preliminary investigation of the facet angles[30] and α-phase orientation of the grains at the fatigue crack initiation site did not provide any clear indication as to the reason for the observed scatter among the remaining four specimens. In the study,[30] it was determined that all of the initiation facets were inclined between 40 and 45 deg to the loading axis and were coincident with the basal plane by using the EBSD/ direct-method tilt fractography technique described earlier. In this investigation, the fatigue crack initiation sites of the shortest life (specimen 1, failed after 736,498 cycles) and the longest life (specimen 2, failed after

4,345,220 cycles) specimens, excluding the subsurface initiation site, were examined in substantial detail to document the factors that could contribute to scatter in fatigue life.

B. *Fractography and Focused Ion Beam Methods*

The as-fractured specimens were coated in an acrylic lacquer (MICCROSTOP*) to protect the fracture sur-

---

*MICCROSTOP is a trademark of MICCRO Products, Tolber Chemical Division, Hope, AR.

---

face and were sectioned perpendicular to the uniaxial loading direction with a wire electrical discharge machine. Following sectioning, the lacquer was removed by ultrasonically cleaning in acetone and finally in isopropyl alcohol followed by drying with a compressed air stream. The specimens were examined optically and then in a scanning electron microscope (SEM) to locate the fatigue crack initiation sites. The initiation sites were prepared for EBSD analysis with a FEI NOVA 600 NanoLab (FEI and NOVA**) equipped with a

---

**FEI and NOVA are trademarks of FEI Company, Hillsboro, OR.

Sidewinder† ion column capable of ion milling at low

---

†Sidewinder is a trademark of FEI Company, Hillsboro, OR

---

accelerating voltages. The samples were oriented such that the facet plane of interest was nearly parallel with the ion beam direction in order to minimize the amount of material that needed to be removed to reveal the underlying microstructure. Initial milling to remove the majority of material was performed at an accelerating voltage of 30 kV and a current of 21 nA to expose a flat surface. Subsequently, a lower-energy 5-kV/1.5-nA milling was performed at a 5-deg incidence to the rough cut surface in order to reduce the amorphous damage layer[32–34] induced by the 30-kV milling step and improve EBSD pattern quality.

C. *Scanning Electron Microscopy/EBSD*

After focused ion beam (FIB) milling, each specimen was put in an SEM equipped with a field emission source and a commercially available EBSD system. The SEM was operated at 20 kV with a beam current of approximately 2.39 nA. The FIB-milled surface was oriented at the EBSD detector in the chamber such that the incident electron beam approached at an angle of 20 deg. This implies that the stage tilt was not 70 deg, which is the conventional choice for EBSD experiments. As a result, it was necessary to modify the settings in the EBSD acquisition software to reflect the true stage tilt in order to properly index the crystallographic orientations

relative to the sample reference frame shown in Figure 1. Depending on the length scale of the constituents at the site under investigation, beam control scans were performed with step sizes of 1, 0.35, or 0.1 μm.

IV. RESULTS AND DISCUSSION

A. *Fatigue Crack Initiation Site of Specimen 1*

The crack initiation site of the shortest-life specimen is shown at increasing levels of magnification in Figures 3(a) through (c). The first grain to crack could be easily identified in the cast material because there was typically one facet that was most prominent and had a microscopically smoother surface than the surrounding facets. The widest dimension of this particular initiation facet was approximately 310 μm. Closer inspection of the first facet to form, Figure 3(c), revealed that there were two sets of distinct linear features present on the facet surface. The first set, designated by (1), is consistent with the "steps" described by Beachem and Pelloux.[35] Wojcik *et al.*[15] observed similar linear features on the fatigue fracture surfaces of single-colony specimens of Ti-811. The steps run back to one edge of the facet that is microscopically smooth compared to other parts on the facet, which identifies this as the crack initiation site. The second set of linear features, denoted by (2) in Figure 3(c), corresponds to the α/β interfaces. There is a distinct change in fracture topography associated with fracture of the β phase. This is evident in Figure 4, which shows a fatigue facet and the adjacent microstructure from a four-point-bend fatigue specimen with a metallographically prepared surface. There is one-to-one correspondence between the β ribs in the microstructure and on the fracture surface, two of which are designated by the letter "A" in Figure 4. In addition, other features from the microstructure are visible on the facet surface. For example, the edge of single-α lamellae is marked by the letter "B" and a similar feature is also evident on the fracture surface. Finely spaced basal slip bands that run parallel to the facet plane are also evident.

The increased surface roughness associated with fracture of the β ribs prohibited determination of its orientation by direct methods. The fracture surface was not as smooth and planar as the α phase and, as a result, it was not possible to get a coherent beam into the lattice beneath the fracture surface that could elastically scatter and subsequently generate EBSD patterns from the β phase. Consequently, it was necessary to use the FIB to remove a small volume of material from the edge of the facet in order to expose the microstructure directly beneath it (Figure 5). The EBSD line scans were performed across the FIB-milled surface to obtain both the α- and β-phase orientations. The appropriate poles have been plotted on equal-angle projections in Figure 6 to explicitly show how the Burgers orientation relationship was satisfied by these measured orientations. Based on the positions of the basal pole and the $\langle a_1 \rangle$, $\langle a_2 \rangle$, and $\langle a_3 \rangle$ directions relative to the loading direction, the Schmid factors were determined to be 0.49, 0.28, and
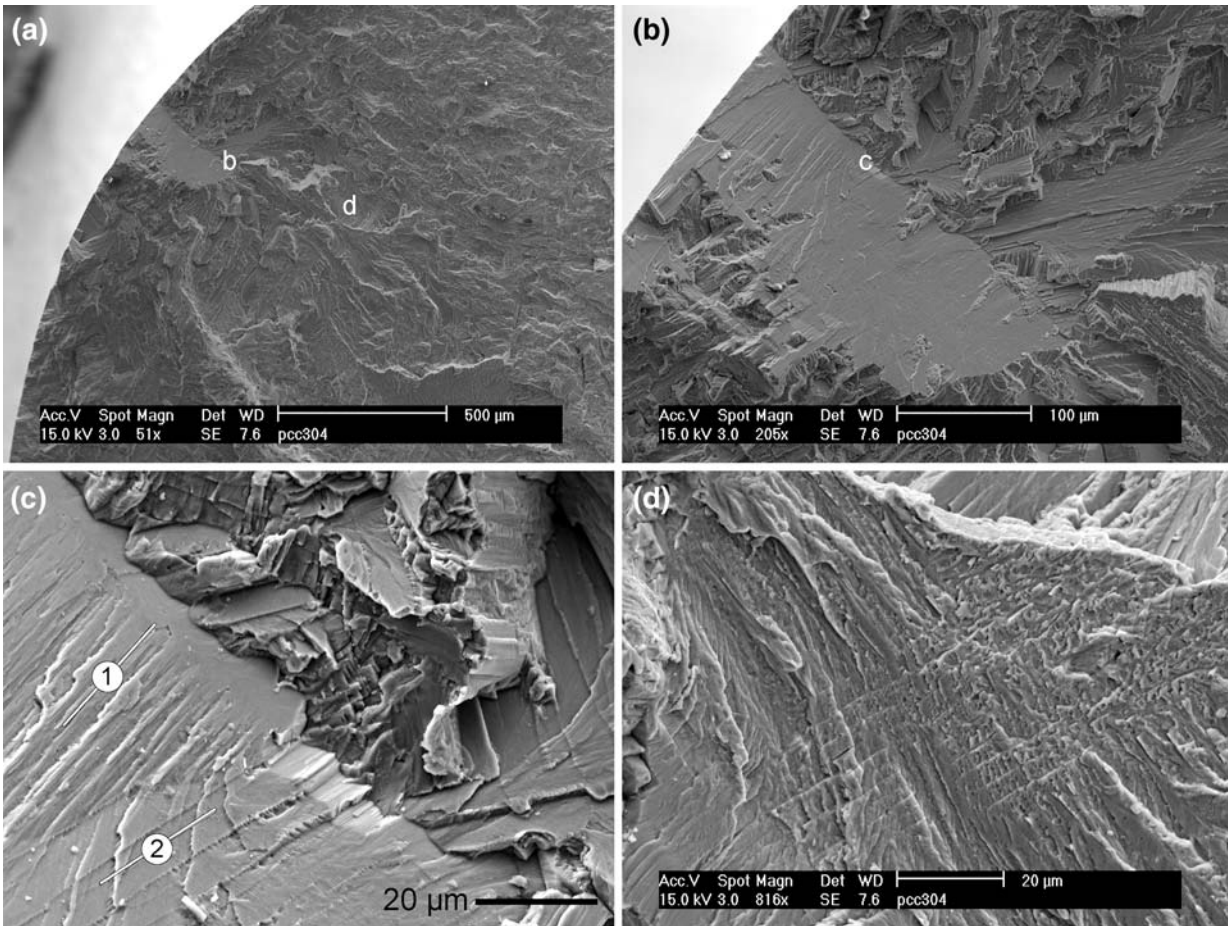
Fig. 3—(*a*) through (*d*) Secondary electron images of the fatigue crack initiation site in specimen 1. White letters in (a) and (b) show locations of higher-magnification images in (c) and (d). The linear features parallel to (1) in (c) are steps, while the linear features parallel to (2) correspond to the α/β interfaces. Image (d) shows the increased surface roughness on facets away from the initiation sites.
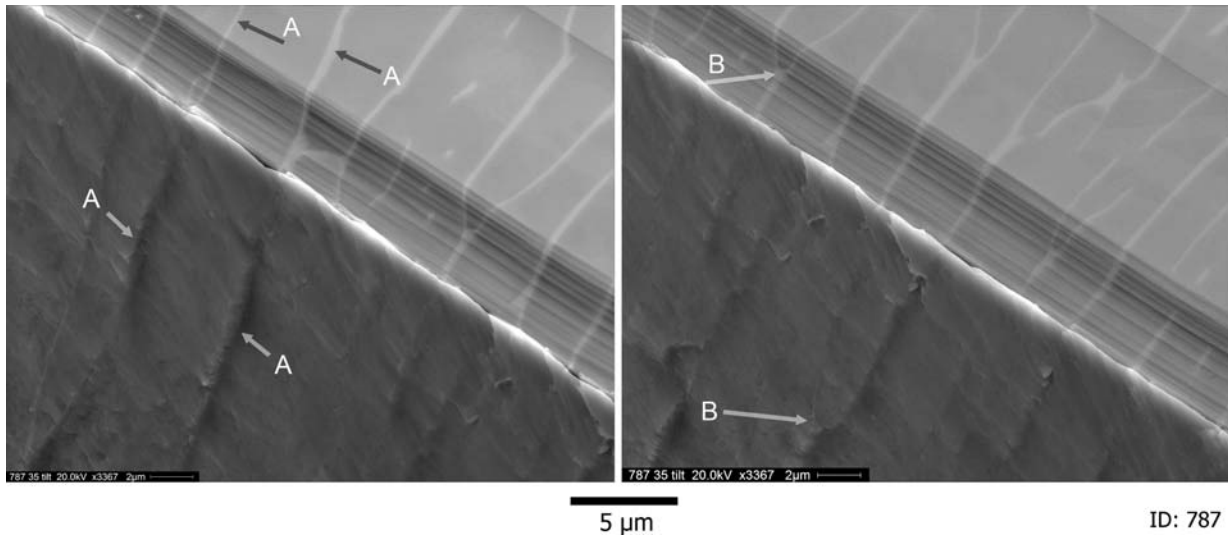

Fig. 4—Fatigue facet and adjacent microstructure on polished surface of a four-point-bend fatigue specimen. Features evident on both polished and facet surfaces have been marked with letters A and B.

0.22, respectively. In order to correlate the measured α- and β-phase orientations with the features on the fracture surface, quantitative tilt fractography has been used to define several vectors on the fracture surface, which are shown in Figure 5. The approach used here is different from previous approaches using quantitative
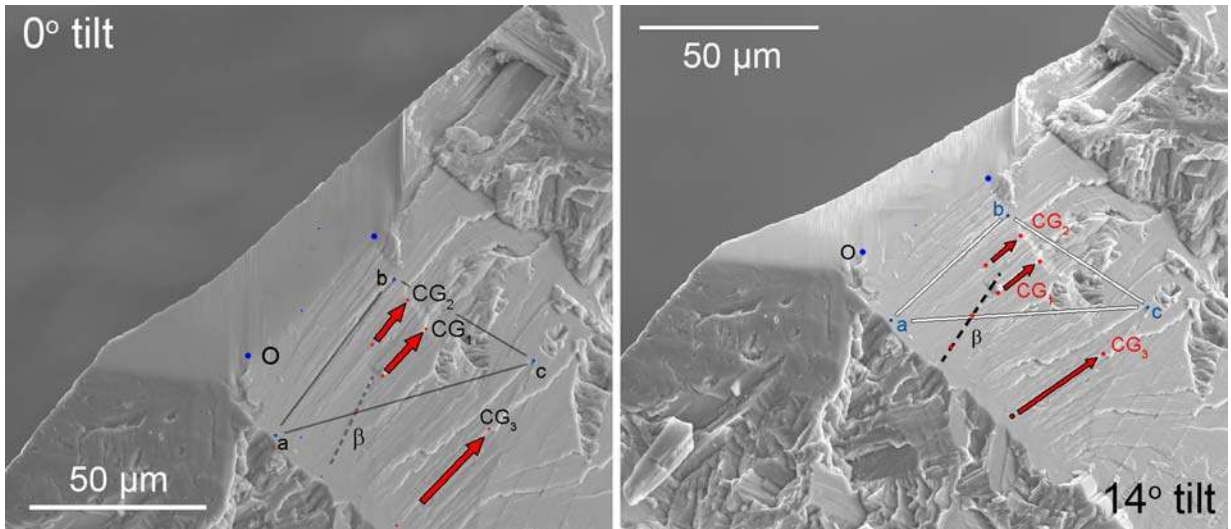
Fig. 5—Crack initiation site shown at tilt angles of 0 and 14 deg after corner has been removed with FIB. Features used for tilt fractography calculations are identified as follows: O is the origin, *abc* identifies the plane of the facet, β is the trace of fractured β lamellae in the plane of the facet, and $CG_{1,2,3}$ are traces of the steps in plane of the facet.
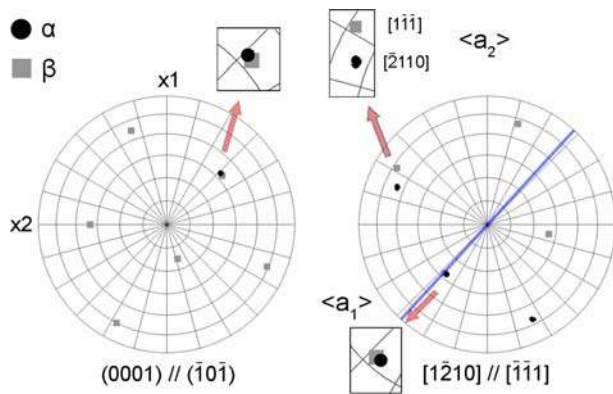

Fig. 6—Equal-angle projections in which basal and 110 poles (left) and 1120 and 111 poles (right) have been superimposed to identify spatial orientation of $\langle a_1 \rangle$, $\langle a_2 \rangle$, and $\langle a_3 \rangle$ in sample reference frame. Lines on pole figures demarcate 15-deg intervals.
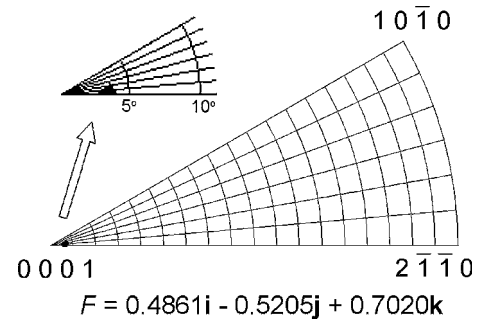

$$F = 0.4861i - 0.5205j + 0.7020k$$

Fig. 7—Equal-angle inverse pole figure corrected for facet normal, **F**, revealing that plane of fracture of specimen 1 is coincident with basal plane within the error associated with the measurement technique.

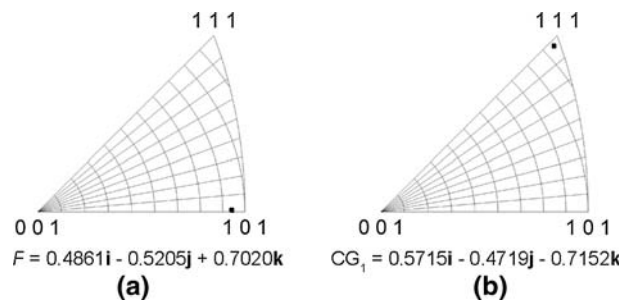$F = 0.4861i - 0.5205j + 0.7020k$ $CG_1 = 0.5715i - 0.4719j - 0.7152k$

(a)   (b)

Fig. 8—Equal-angle inverse pole figures depicting orientation of β phase relative to (a) facet normal and (b) vector CG_1.

Table I.   Results from Quantitative Tilt Fractography Measurements Corresponding to Features Identified in Figure 5

Feature	Unit Vector Describing Feature
Macroscopic fracture plane normal	$\mathbf{ab} \times \mathbf{bc} = \mathbf{F} = 0.4861\mathbf{i} - 0.5205\mathbf{j} + 0.7020\mathbf{k}$
Trace of step	$\mathbf{CG_1} = 0.5715\mathbf{i} - 0.4719\mathbf{j} - 0.7152\mathbf{k}$
Trace of step	$\mathbf{CG_2} = 0.5436\mathbf{i} - 0.4282\mathbf{j} - 0.7219\mathbf{k}$
Trace of step	$\mathbf{CG_3} = 0.5242\mathbf{i} - 0.4996\mathbf{j} - 0.6896\mathbf{k}$
Trace of β rib in facet plane	$\boldsymbol{\beta} = 0.6969\mathbf{i} - 0.3514\mathbf{j} - 0.6252\mathbf{k}$

tilt fractography[1–3,8] in that vectors have been strategically placed to coincide with distinctive linear features that lie within the plane of the facet. The results of the tilt fractography calculations are shown in Table I. The cross product of vectors **ab** and **bc** yields the facet

normal, **F**, which made an angle of 45.4 deg with the loading direction. The vector parallel to the trace of the β phase on the fracture surface is designated by the dashed line $\boldsymbol{\beta}$, while three vectors that are parallel to the steps on the facet surface are given by $\mathbf{CG_1}$, $\mathbf{CG_2}$, and $\mathbf{CG_3}$. The plane of fracture was determined by plotting
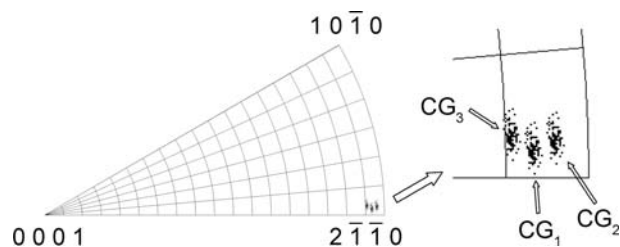
Fig. 9—Equal-angle inverse pole figure showing orientation of α phase relative to long axis of steps designated by **CG₁**, **CG₂**, and **CG₃** in Fig. 5.

an inverse pole figure relative to **F**, as shown in Figure 7. In this plot, all of the discrete α orientations measured from the FIB-milled surface are shown to reveal the typical angular spread encountered for these measurements. In this sample, the fracture plane was less than 3 deg from the basal plane, which is within the experimental error of the technique. A similar analysis was performed on the β-phase orientation that was measured with EBSD and it was found that the macroscopic plane of fracture corresponded to {110} (Figure 8). With regard to the steps in the plane of the facet, the α-phase orientation was plotted relative to the three **CG** vectors in Figure 9. All three were within ~5 deg from the normal to the $\{2\bar{1}\bar{1}0\}$ plane, which is equivalent to saying that all three are within ~5 deg from the $\langle 2\bar{1}\bar{1}0\rangle$ direction, according to Eq. [6]. This was further verified by analyzing the relation between the β-phase orientation and the long axis of the steps on the facet surface (Figure 8). Because the use of an inverse pole figure reduces the measured orientation into the unit triangle, this analysis does not make explicit which $\langle 2\bar{1}\bar{1}0\rangle$ direction is parallel to the steps, *i.e.*, $\langle a_1\rangle$, $\langle a_2\rangle$, or $\langle a_3\rangle$. There are, however, two methods by which this can be determined. In the first, the trace of the steps can be taken from an image acquired at 0-deg tilt and superimposed onto the pole figures depicting the α- and β-phase orientations (blue line in Figure 6). The trace of the step will intersect the $\langle a\rangle$ direction that is parallel to it. In the second method, for a more rigorous analysis, the crystallographic and morphological relationships imposed by the Burgers orientation relationship can be used to make the identification. This method also serves as a way to perform a self-consistent check between the vectors determined with tilt fractography and the crystallographic orientations measured with EBSD. The macroscopic α/β interface, also known as the lattice-invariant line, is parallel to the $\langle 335\rangle_\beta$ direction that is nearest to the $\langle a_1\rangle$ direction.[17,22,26,36] Thus, the trace of the β rib on the facet surface should be located ~14.4 deg from the $\langle a_1\rangle$ direction (Figure 2). Although the exact angle is dependent on the precise c/a ratio,[36] the difference is small compared to the resolution of the tilt fractography/EBSD technique. The $\langle a_1\rangle$ direction measured by EBSD was transformed to a unit vector in the sample reference frame and compared to the **CG** vectors determined from tilt fractography. The angles between $\langle a_1\rangle$ and **CG₁**, **CG₂**, and **CG₃** were determined to be 13.6, 11.7, and 13.8 deg, respectively, which is in

agreement with the theoretical angle of 14.4 deg within the tolerance of the tilt fractography/EBSD technique.

B. *Fatigue Crack Initiation in Specimen 2*

The planar facet at the crack initiation site of the longer-life specimen also had a normal that was 45 deg relative to the primary loading axis, and so its orientation could not be used to account for the difference in fatigue life relative to specimen 1. The total facet length was approximately 40 pct less than that of specimen 1, with its largest dimension measuring 180 μm. Eylon[28] has shown that larger initiation sites generally correspond to shorter total fatigue life in investment-cast and hot isostatically pressed Ti-6Al-4V, which can account for a part of the longer fatigue life of this specimen. Compared to specimen 1, a larger portion the initiation site of specimen 2 was removed by FIB milling in order to investigate a larger area of the microstructure beneath the fracture surface (Figure 10). The area was imaged with secondary electrons at two different tilt angles in order to facilitate the tilt fractography calculations, while the microstructure was imaged with backscattered electrons at −1-deg tilt. The backscattered electron image revealed that there were multiple colonies present directly beneath the fracture surface. The facet plane remains constant across many of these colonies; however, two of the colonies cause discontinuities where they intersect the facet plane.

The underlying microstructure was further investigated by EBSD to determine the crystallographic orientation of the primary facet and the surrounding microstructure. The EBSD data have been colored with respect to the loading direction according to the unit triangle in Figure 11. In addition, the orientations have been expressed as Bunge Euler angles,[37] in which the hcp unit cell has been attached to the sample reference frame using Nye's convention.[38] In this figure, each unique variant of the Burgers orientation relationship is labeled by an integer. Thus, it is possible for two colonies that are not touching to be the same number. The colonies in the orientation designated by the number 4 in Figure 11 contain both pink and purple hues in the EBSD map. This was caused by an error during the automated indexing of the EBSD patterns, however; only the pink orientation maintains the proper Burgers-related α-phase misorientations with all of the adjacent colonies and thus must be the orientation for this particular colony. There are several notable relationships among these colonies. For example, colonies 1 and 2 share a common basal plane but are rotated 10.5 deg about [0001] relative to one another. Colonies 3, 4, and 6 all have basal planes that are approximately 60 deg away from that of colony 1 and 2; however, these rotations are about different axes. Colony 5, on the other hand, had its basal plane at 90 deg to colonies 1 and 2. The orientations are shown in the unit triangle with respect to the loading and facet-normal directions in Figure 11. From the latter, it was identified that the fracture plane was parallel to the basal plane in colonies 1 and 2, was within approximately 10 deg from the $\{10\bar{1}0\}$ plane in colony 5, and was near a $\{10\bar{1}1\}$ plane
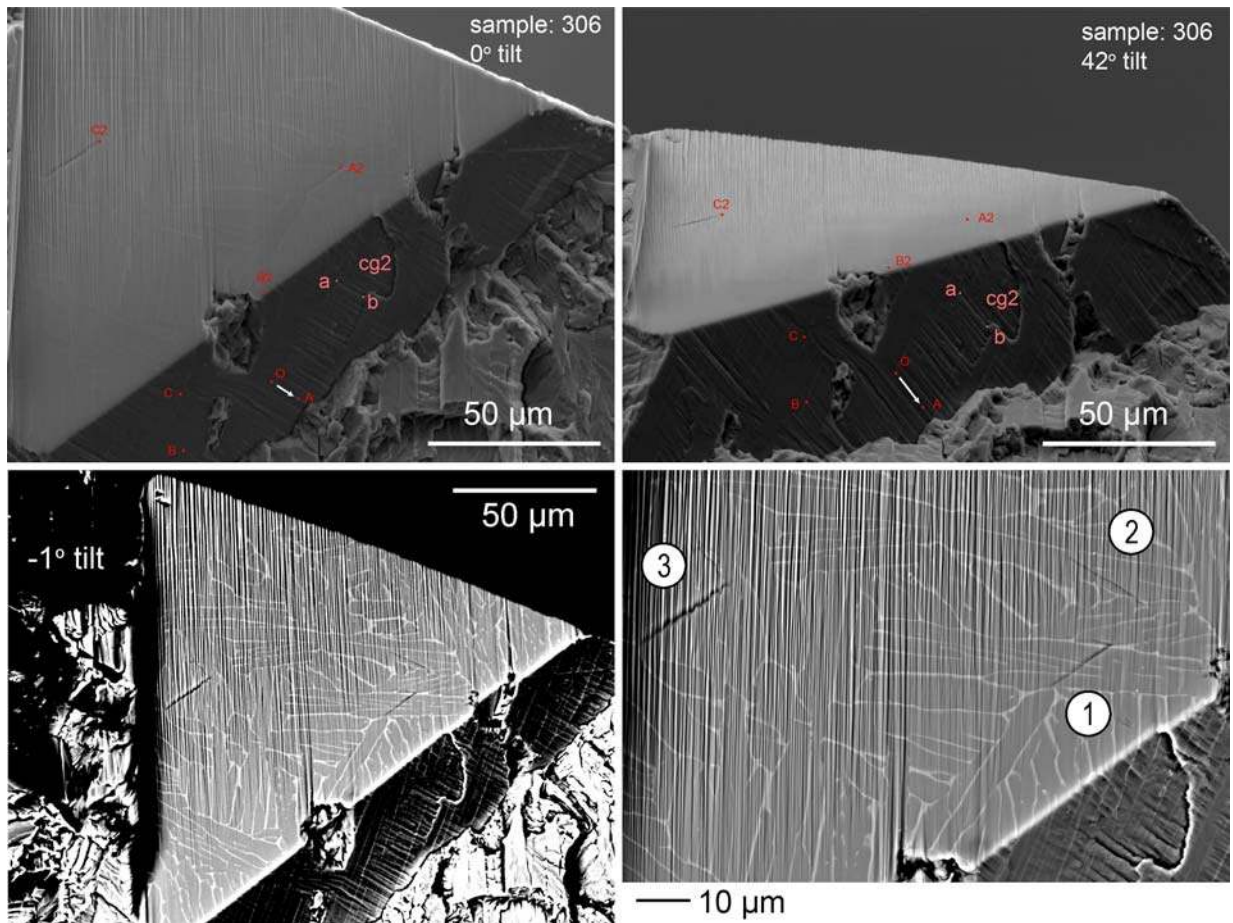
Fig. 10—Faceted initiation site of specimen 2 with upper half removed by FIB milling to reveal underlying microstructure. Points labeled on images were used for tilt fractography calculations.

in colonies 3 and 4. The discontinuities in the facet plane occurred where it was intersected by colonies 4 and 6, which did not share a common basal plane with colonies 1 and 2. The process by which these colonies fractured appeared to be a ductile tearing mechanism that occurred after faceted growth in colonies 1 and 2 left small ligaments of colony 3 and 4 connecting to two halves of the fracture surface. A similar mechanism, in which cracks grow faster through grains in some orientations than in others, has been shown to occur at longer crack lengths in Ti-6Al-4V by Bowen.[39]

The β-phase orientation was not resolved with any confidence at the level of resolution at which the EBSD scan was performed; however, there were more than enough unique α variants present to calculate the β-phase orientation by assuming the Burgers orientation relationship was held during the $\beta \rightarrow \alpha$ transformation. The parent β orientation, calculated using the method of Glavicic et al.,[40,41] is shown in Figure 12. Based on the knowledge of the calculated β orientation, the fracture plane was verified as being coincident with {110}. The traces of the steps on the facet surface were found to be parallel to the $\langle a_2 \rangle$ direction as opposed to the $\langle a_1 \rangle$ direction observed in the shorter-life specimen 1. In the case of specimen 2, it was possible to make this

determination using a three-dimensional approach as opposed to the "in-plane only" measurements from specimen 1, which only considered the lattice-invariant line and not the true β-platelet normal. It was assumed that the β phase could be represented as a two-dimensional platelet defined by its traces on the facet surface and the FIB-milled surface, which were determined with quantitative tilt fractography. The angle between the β-platelet normal and the approaching α-phase slip system, β_b by Chan's definition,[16,19] was determined to be 18 deg for specimen 2. This is in good agreement with the theoretical value of 15 deg for $\langle a_2 \rangle$ slip, which is also said to be the most difficult of the basal slip systems to activate.[19]

It is interesting to note that the β-phase orientation in specimen 2 is similar to that in specimen 1; a simple rotation of ~70 deg about the direction normal to the plane of the projections in Figure 6 brings the 110 and 111 poles nearly coincident with those in Figure 12. This rotation is arbitrary because the grains are only concerned with one direction in an axial test. Thus, the orientation of the β phase in the first grain to crack was essentially the same in both samples. The orientation with respect to axial loading is such that there is substantial resolved shear stress on 8 of the 12
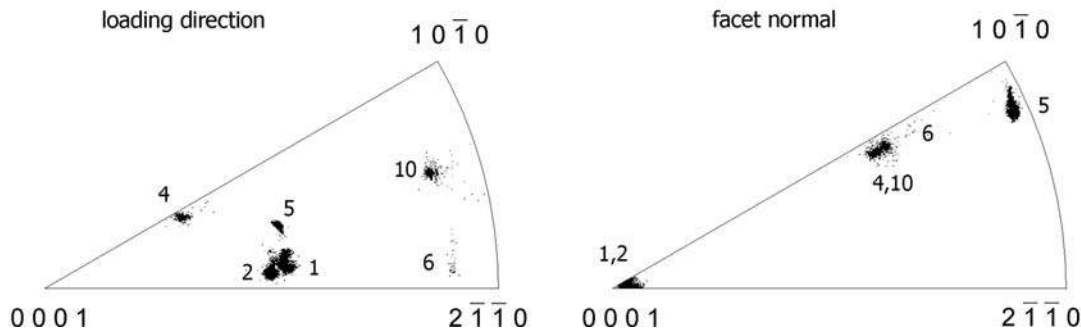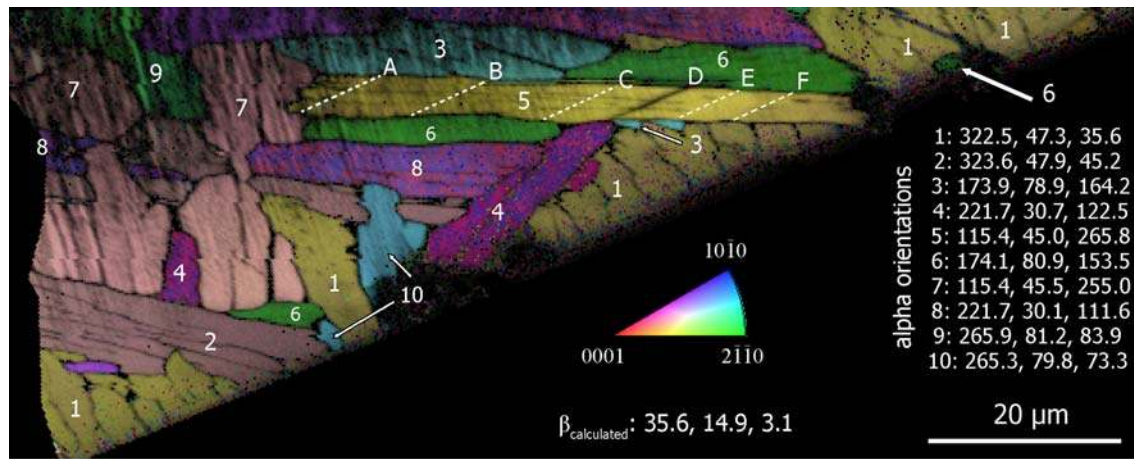
Fig. 11—EBSD and image-quality map of microstructure revealed by FIB milling. Average orientations of several of the unique variants of Burgers orientation relationship relevant to the present discussion are expressed as Euler angles as well as on equal-area inverse pole figures. Trace of the basal plane in colony 5 is marked at several locations by dotted lines. (See text for additional details.).
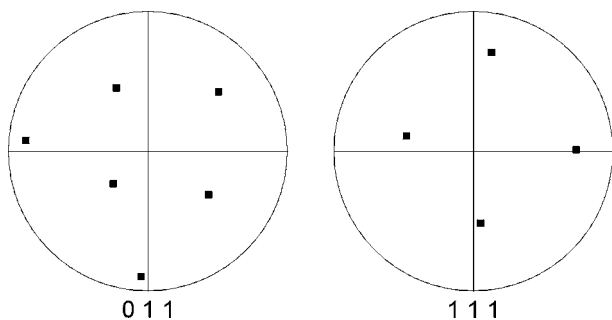

Fig. 12—β-phase orientation calculated from the inherited α variants shown in Fig. 11. The loading direction is normal to the plane of the projection.

$\{110\}\langle111\rangle$ slip systems, implying there is a high probability for basal slip within this colony. The slip system or slip systems that will operate during loading depend on a crystallographic and geometric criterion that has been described by Chan.[19] In his analysis, Chan has shown that the angle between the β-platelet normal and the incident α-phase slip direction strongly influences the activation of slip systems in single colonies. However, during cyclic loading, when the applied stresses are well below the macroscopic yield point, unlike those single colonies studied by Chan et al.[16] and Chan,[19] and the slip systems are repeatedly stressed which may cause deviation from the uniaxial

tension through yielding model. Moreover, Chan's analysis is meant to explain a failure of Schmid's law for titanium alloys with lamellar microstructures. However, in this case, the steps on the facet surface were parallel to the slip system with the highest Schmid factor, suggesting these were the operative slip systems. These results are consistent with those of Bridier et al.[11] who observed that Schmid's law is more frequently obeyed during cyclic loading of Ti-6-4 than during monotonic loading.

1. Effect of local crystallographic orientation on fatigue crack initiation

Three small cracks that were revealed by FIB milling are identified in the backscattered electron images in Figure 10. Because it is not possible to detect and arrest such small cracks using potential drop methods or compliance methods, the FIB milling technique has provided a unique opportunity to study naturally occurring fatigue cracks at their smallest scale without being plagued by the question of how the plane-stress condition at free surfaces affects crack initiation when observing crack formation in polished specimens.[11,13,42] Cracks 1, 2, and 3 formed within colonies given by the orientations 5, 8, and 7, respectively, in Figure 11. Trace analysis and correlation with EBSD data showed that all of the cracks revealed by FIB milling were parallel to the basal plane in their respective colonies. The available basal slip length in the colonies containing each of these

cracks was significantly less than that of the primary facet. While each crack formed within a colony of a different orientation, they all shared some similarities. For example, the colonies containing cracks 1 and 3 both had basal poles that made an angle of 46 deg to the primary loading direction, which is consistent with the angles made by the primary crack initiation sites that eventually propagated to failure. On the other hand, the basal pole in the colony containing crack 2 made an angle of 31 deg with the primary loading direction. This is consistent with previous work that showed the faceted initiation sites in continuous cyclically loaded titanium alloys typically have their basal poles inclined 25 to 45 deg to the loading axis,[11–14] which results in a combination of shear and normal stresses resolved on the basal plane. Specimens with large slip lengths tended to favor orientations with higher resolved shear stress, *i.e.*, where the facet angles are closer to 45 deg, while finer structures tend toward the 25- to 35-deg range. The shear stress is required for dislocations to glide on the basal plane, while the resolved normal stress is the mode I opening component required to cause decohesion of the slip band.[43] Therefore, a first attempt at identifying colonies that are crystallographically suited for fatigue crack initiation can be made based on a fairly simple criterion: locating those colonies that have both high resolved shear stress and high resolved normal stress on the basal plane. The relative amount of normal force resolved on the basal plane can be reduced to a scalar parameter by taking the absolute value of the dot product between a unit vector, $\mathbf{b_n}$, parallel to [0001] and a unit vector, $\mathbf{k}$, parallel to the loading direction. The amount of shear stress resolved on the basal plane is proportional to the Schmid factor. Thus, the initial search for colonies in an orientation favorable for initiation can be made with Eq. [7]:

$$N = |\mathbf{b_n}\cdot\mathbf{k}|m_{max} \qquad [7]$$

$|\mathbf{b_n}\cdot\mathbf{k}|$ varies between 0 and 1 for a grain that has its basal pole perpendicular and parallel to the loading direction, respectively, while m_{max} varies between 0 and 0.5 when the basal pole is parallel and 45 deg relative to the loading direction, respectively. Thus, higher values of N correspond to grains that have the required combination of forces resolved on the basal plane that have been found to promote crack formation. While it is recognized that the grain-level stress state is actually orientation dependent and does not necessarily match the applied "uniaxial" stress state,[44] a simplified analysis of this nature can be used as a first approximation. Imposing this criterion on the orientations presented in Figure 11 identified all of the colonies that formed cracks, namely 1, 2, 5, 7, and 8. These colonies all had values of N between 0.32 and 0.36, while those that did not form cracks were generally less than 0.05. However, this criterion also identified colonies in orientation 4 (this is related by 10.5 deg about [0001] to orientation 8, in which cracks were observed) and, furthermore, does not provide any indication of where in the microstructure the cracks will form. In this regard, the crack in colony 5 was of interest because it was bordered by a single lath of a different orientation on the bottom, as shown in Figure 13. While not an absolute certainty, logic dictates that because the crack borders this lath, as opposed to any of the other possibilities, it was influential to the crack initiation process. On the other side of colony 5, the crack propagated through the β phase and into colony 6, then turned sharply and propagated parallel to the α/β interface in colony 6 and was apparently arrested. The crystallographic orientations of the colonies surrounding this crack were investigated in detail and are discussed in this section and briefly compared to the two others revealed by FIB milling.

Inspection of Figure 11 reveals that there are five unique colony orientations that could border a basal slip
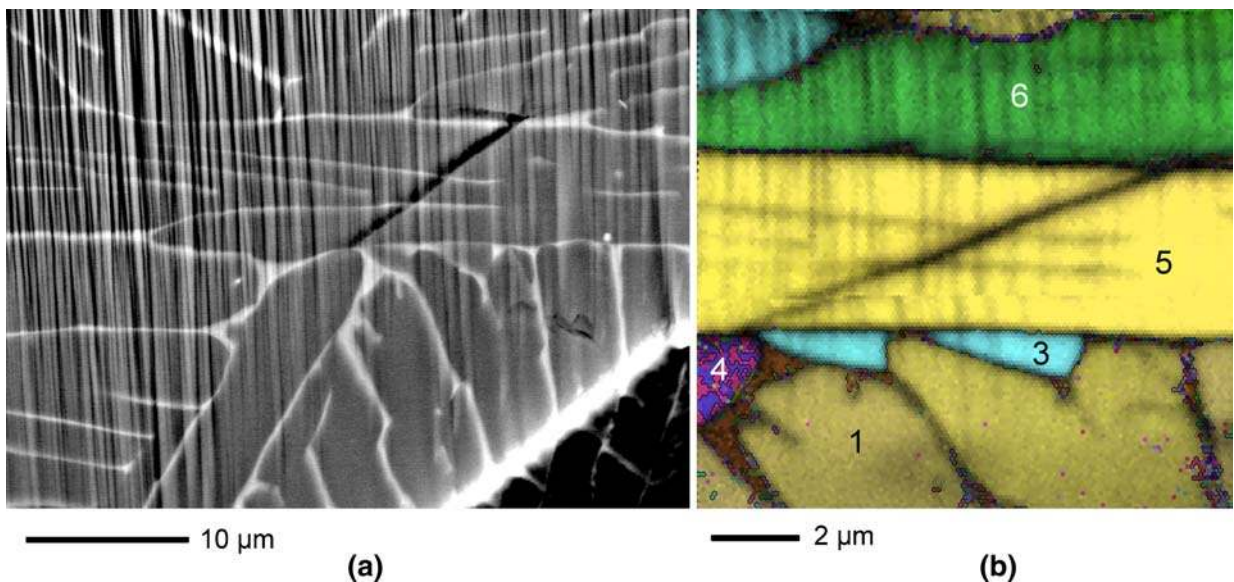

Fig. 13—(*a*) Backscattered electron image and (*b*) inverse pole figure colored EBSD map of microstructure surrounding submerged crack.
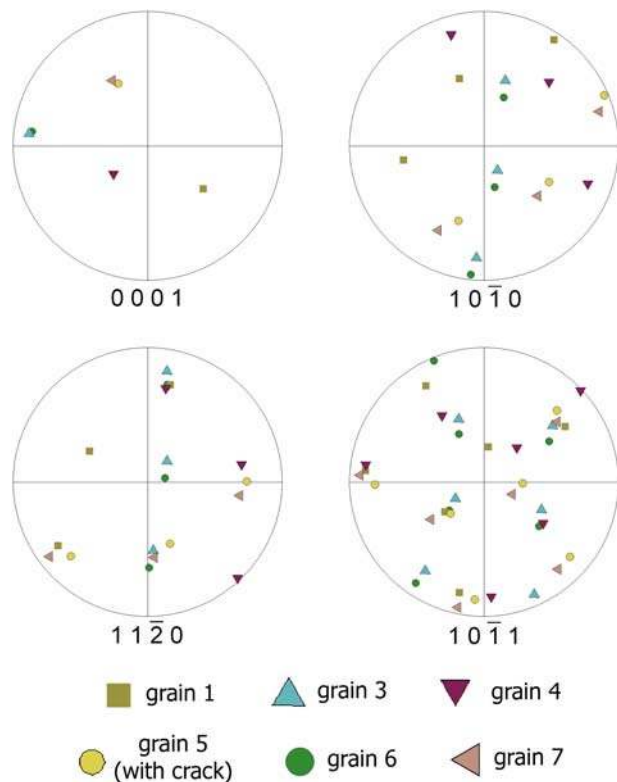
Fig. 14—Discrete equal-angle pole figures showing α-phase orientations of colony 5 and its neighbors. The 0001 and $11\bar{2}0$ poles can be compared with 110 and 111 poles, respectively, of β phase in Fig. 12 to identify $\langle a_1 \rangle$, $\langle a_2 \rangle$, and $\langle a_3 \rangle$ slip directions in each colony. The loading direction is perpendicular to the plane of the projection.

band in colony 5. However, there are six possible combinations of nearest neighbors for a basal slip band in colony 5, the traces of which are designated by dashed lines and labeled A, B, C, E, and F in Figure 11. The crack formed at the sixth possibility, designated D, which appears black in this image because of the grayscale image quality[45] map that was overlaid onto the colored orientation map. Image quality is a measure of EBSD pattern quality, which is extremely poor when the electron beam is incident on the crack. The orientations of the colonies are shown on the 0001, $10\bar{1}0$, $11\bar{2}0$, and $10\bar{1}1$ pole figures in Figure 14. This figure clearly identifies the coincidence of both similar and dissimilar {hkil} slip planes among adjacent Burgers-related colonies. The former is evident by overlapping points in the same pole figure, while the latter is observed by superimposing the 0001 and $10\bar{1}1$ pole figures, for example. These coincidences are important because observations of α-colony boundaries in the SEM revealed that α/α boundaries are often formed where laths meet and there is not necessarily retained β phase between them. Thus, it is possible for slip to transfer to occur directly across α-colony boundaries without the need for transmission through the β phase.

In order to quantitatively assess the coincidence of slip planes in adjacent Burgers-related α colonies, the parameter proposed by Luster and Morris[46] has been used. In this analysis, the alignment of slip systems is

reduced to a scalar parameter m' by taking the product of the cosine of the angle ψ between the slip plane normal in each colony and the cosine of the angle κ between the Burgers vectors:

$$m' = \cos \psi \cos \kappa \qquad [8]$$

Thus, m' is nondirectional and, as the angle between the slip plane normals approaches zero and as the angle between the slip directions approaches 0, m' approaches 1. This is indicative of a boundary that is crystallographically suited for slip transfer. Of course, there are morphological dependences as well,[47–51] such as the grain boundary inclination with respect to the loading axis, but m' does not account for them. A total of 18 slip systems were considered in each colony: 3 basal, 3 prism, and 12 first-order pyramidal slip systems. In general, at room temperature, the CRSS for the prism slip system is the smallest, followed closely by the basal slip. Pyramidal $\langle c + a \rangle$ slip has between 2 and 5 times higher CRSS[52,53] and, thus, is not readily activated at the relatively low stresses imposed during high-cycle fatigue loading.[11] For the present analysis, the orientation of colony 5 was considered as the reference and m' was calculated for all 18 slip systems in each of the 5 unique orientations bordering it. Of the 1620 sampled slip-system combinations, only 44 (2.72 pct) had $m' > 0.90$, while 104 (6.42 pct) had $m' > 0.75$. These numbers reduce further to 1.60 and 5.31 pct, respectively, if the 18 nearly coincident slip systems in colony 7 are not considered in the calculation. Recall that colonies 5 and 7 are related by 10.5 deg about [0001] and, because the cosine of 10.5 deg is 0.983, all 18 slip systems will have m' between 0.96 and 0.98. As shown in Table II, which summarizes all slip systems with $m' > 0.90$, there were only two that had $m' = 1.0$.

2. Phenomenological model for high cycle fatigue crack initiation

The near coincidence between the basal $(0001)\langle a_2 \rangle$ in colony 5 and $(10\bar{1}1)[11\bar{2}\bar{3}]$ in colony 4 is of particular interest, because this is the boundary at which the crack initiated. This is especially true, because grains with parallel basal and first-order pyramidal planes were recently observed at the crack initiation site of a Ti-6Al-4V sample with a bimodal microstructure.[13] For the simple case of perfect alignment between the slip systems, in order for a dislocation to transfer from the basal plane across the α/α-colony boundary and onto the first-order pyramidal slip system in an adjacent colony, a residual boundary dislocation must be formed through the reaction:

$$1/3\langle 2\bar{1}\bar{1}0 \rangle + 1/3\langle 11\bar{2}\bar{3} \rangle \rightarrow [0001] \qquad [9]$$
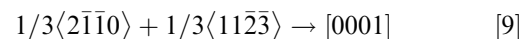
If multiple $\langle c \rangle$ dislocations, which are perpendicular to the basal plane, are created in the grain boundary, it is possible that a crack could nucleate within the boundary and propagate back along the basal slip band by faceted growth.[12] As mentioned by Blackburn and Williams,[54] the dislocation reaction in Eq. [9] is analogous to creating a [001] superdislocation in a bcc material. The formation of such a dislocation has been linked to

Table II. Slip Systems That Are Coincident or Nearly Coincident with Those in Colony 5 in Which the Crack Started

m'	Slip Systems in Adjacent Colony	Adjacent Colony	Slip Systems in Reference Colony 5	Angle/Axis Pair
0.98	$(10\bar{1}0)\,[1\bar{2}10]$	1	$(0001)\,[\bar{1}2\bar{1}0]$	90 deg/$\langle 1\,\overline{2.38}\,1.38\,0 \rangle$
0.91	$(1\bar{1}01)\,[1\bar{2}1\bar{3}]$		$(0\bar{1}10)\,[\bar{2}110]$	
0.93	$(\bar{1}101)\,[1\bar{2}1\bar{3}]$		$(\bar{1}100)\,[\bar{1}1\bar{2}0]$	
0.98	$(0001)\,[\bar{1}2\bar{1}0]$		$(10\bar{1}0)\,[1\bar{2}10]$	
0.93	$(0001)\,[2\bar{1}\bar{1}0]$		$(01\bar{1}1)\,[1\bar{2}1\bar{3}]$	
0.92	$(\bar{1}100)\,[\bar{1}1\bar{2}0]$		$(0\bar{1}11)\,[1\bar{2}1\bar{3}]$	
1.00	$(1\bar{1}01)\,[1\bar{2}1\bar{3}]$	3	$(0001)\,[11\bar{2}0]$	60.83 deg/$\langle \overline{1.377}\,\bar{1}\,2.377\,0.359 \rangle$
0.90	$(1\bar{1}01)\,[2\bar{1}\bar{1}3]$		$(0001)\,[\bar{1}2\bar{1}0]$	
0.97	$(0001)\,[2\bar{1}\bar{1}0]$		$(01\bar{1}1)\,[1\bar{2}1\bar{3}]$	
0.93	$(0001)\,[\bar{1}2\bar{1}0]$		$(10\bar{1}1)\,[11\bar{2}\bar{3}]$	
0.98	$(\bar{1}101)\,[1\bar{2}1\bar{3}]$		$(0\bar{1}11)\,[1\bar{2}1\bar{3}]$	
0.98	$(\bar{1}011)\,[2\bar{1}1\bar{3}]$		$(0\bar{1}11)\,[\bar{1}\bar{1}23]$	
0.94	$(10\bar{1}0)\,[1\bar{2}10]$		$(10\bar{1}1)\,[2\bar{1}\bar{1}3]$	
0.97	$(10\bar{1}1)\,[11\bar{2}\bar{3}]$	4	$(0001)\,[2\bar{1}\bar{1}0]$ basal $\langle a_2 \rangle$	60.83 deg/$\langle \overline{1.377}\,\bar{1}\,2.377\,0.359 \rangle$
0.93	$(10\bar{1}1)\,[2\bar{1}\bar{1}3]$		$(0001)\,[\bar{1}2\bar{1}0]$ basal $\langle a_3 \rangle$	
0.93	$(0\bar{1}11)\,[1\bar{2}1\bar{3}]$		$(10\bar{1}0)\,[1\bar{2}10]$	
0.98	$(\bar{1}011)\,[2\bar{1}1\bar{3}]$		$(1\bar{1}01)\,[2\bar{1}\bar{1}3]$	
0.98	$(\bar{1}011)\,[\bar{1}\bar{1}23]$		$(1\bar{1}01)\,[1\bar{2}1\bar{3}]$	
0.91	$(0001)\,[11\bar{2}0]$		$(\bar{1}011)\,[\bar{2}11\bar{3}]$	
1.00	$(0001)\,[2\bar{1}\bar{1}0]$	6	$(\bar{1}101)\,[\bar{1}2\bar{1}\bar{3}]$	63.26 deg/$\langle \overline{10}\,5\,5\,3 \rangle$
0.99	$(1\bar{1}01)\,[1\bar{2}1\bar{3}]$		$(0001)\,[11\bar{2}0]$	
0.93	$(01\bar{1}1)\,[11\bar{2}\bar{3}]$		$(10\bar{1}0)\,[1\bar{2}10]$	
0.98	$(0001)\,[2\bar{1}\bar{1}0]$		$(0\bar{1}11)\,[\bar{1}\bar{1}23]$	
0.92	$(\bar{1}101)\,[\bar{1}2\bar{1}\bar{3}]$		$(0\bar{1}11)\,[1\bar{2}1\bar{3}]$	
0.94	$(\bar{1}011)\,[\bar{2}11\bar{3}]$		$(0\bar{1}11)\,[\bar{1}\bar{1}23]$	
0.94	$(10\bar{1}0)\,[1\bar{2}10]$		$(1\bar{1}01)\,[2\bar{1}\bar{1}3]$	
0.96 to ~0.98	all	7	all (see text for details)	10.5 deg/[0001]

cleavage crack formation on the {100} plane perpendicular to its Burgers vector, as discussed by Cottrell[55] and Suresh.[31] While it is true that faceted growth is distinct from the cleavage cracking in terms of crack propagation,[12] it is possible that the actual crack initiation mechanism is similar. Faceted growth proceeds in a stable manner cycle by cycle at low applied ΔK, whereas cleavage crack growth occurs rapidly and unstably.

The detailed analysis presented above is briefly compared to the other two submerged cracks revealed by FIB milling. The second crack was observed to form within a colony the orientation of which is given by the number 7 in Figure 11. This colony was bordered by others with orientations 8 and 9, although the crack appeared to start on the 7/8 border, was deflected at the 7/9 border, and began to propagate parallel to the colony boundary, similar to the crack previously discussed in detail. Considering the 7/8 colony boundary, it is again observed that the $\langle a_1 \rangle$ slip system in the colony 7 orientation has an m' of 1.00 with the $(10\bar{1}1)\,[11\bar{2}\bar{3}]$ slip system in the adjacent colony 8, and both slip systems

had a Schmid factor of 0.48. The angle/axis misorientation associated with this colony boundary is also 60.83 deg/$\langle \overline{1.377}\,\bar{1}\,2.377\,0.359 \rangle$, making this an identical boundary to that which initiated the crack discussed previously between colonies 4 and 5. Finally, the third crack revealed by FIB milling formed in a colony with an orientation given by number 8 in Figure 11. The crack had not yet propagated all the way across the colony and, therefore, it was concluded that initiation occurred at a boundary with a colony in orientation 6. The two colonies were related by a 63.26-deg rotation about a $\langle \overline{10}\,5\,5\,3 \rangle$ axis. Analyzing the coincidence of slip systems using Eq. [8] revealed that the basal $\langle a_1 \rangle$ slip system in colony 8 had an m' of 1.00 with $(0\bar{1}11)\,[1\bar{2}1\bar{3}]$ in colony 6 and, therefore, this was also a boundary suited for slip transfer from the basal to the first-order pyramidal system.

In summary, this section has analyzed three different cracks that were revealed by FIB milling. The cracks were not influenced by sample surface effects, including any compressive residual stresses that could have been

induced during sample preparation or plane-stress conditions resulting from the free surface. All three cracks were formed in colonies with unique orientations; however, some similarities among the colonies were also observed. In particular, the following were found: (1) the crack planes were parallel to the trace of the basal plane in their respective colonies, (2) the relative amounts of normal and shear stress resolved on the basal planes were similar, and (3) the cracks formed at locations in the microstructure at which these basal slip systems were aligned or nearly aligned with a $\{10\bar{1}1\}\langle11\bar{2}3\rangle$ slip system in an adjacent grain.

C. Observations on Long Fatigue Crack Growth

While the early stages of fatigue crack growth (stage I) commonly occur along crystallographic planes, stage II crack growth is generally insensitive to crystallographic
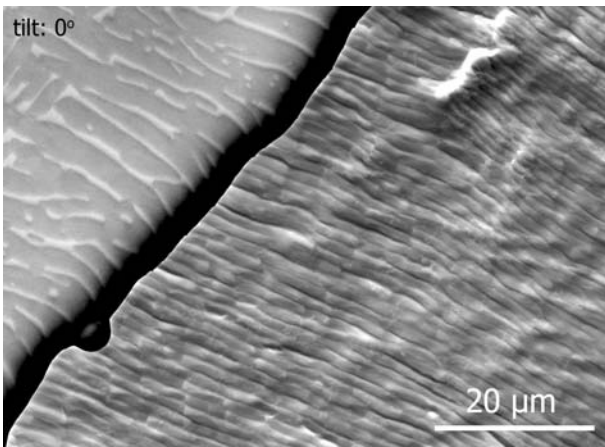

Fig. 15—Fatigue striations and underlying microstructure that was revealed by electropolishing.

orientation in cubic materials.[31] Thus, the fracture surface is generally perpendicular to the applied loading direction in stage II growth in order to maximize the mode I component acting on the crack tip and increase its energy release rate. Fatigue striations are among the most recognizable features formed during stage II growth. They are produced in a wide range of materials and can give an indication of the local crack growth rate as well as the total number of cycles spent during propagation. In this section, we investigate the crystallography of classical fatigue striations formed during long fatigue crack growth in investment-cast Ti-6Al-4V. Due to the large amount of plastic deformation associated with the formation of fatigue striations and their shape, it is not possible to acquire EBSD patterns directly from the fracture surface. Therefore, the selective electropolishing technique reported by Chesnutt and Spurling[56] was used to reveal the microstructure underlying the fracture surface. Briefly, selected areas of the fracture surface were coated with an acrylic lacquer, leaving some parts exposed. The exposed fracture surface was electropolished using an electrolyte containing (by volume) 59 pct methanol, 35 pct butanol, and 6 pct perchloric acid at $-35\,^{\circ}$C at 30 V. The electropolishing time depended on how much material was to be removed, but 15 seconds was generally sufficient to remove approximately 3 to 5 μm of material, which revealed the underlying microstructure. Electropolishing is the ideal method for preparing EBSD samples, because mechanically induced surface deformation is eliminated, resulting in increased EBSD pattern quality. One area that was analyzed in detail is shown in Figure 15. In this image, the microstructure was imaged with backscattered electrons to enhance the atomic number contrast of the two phases, while the fracture surface has been imaged with secondary electrons to enhance surface topography. It can be seen that the β
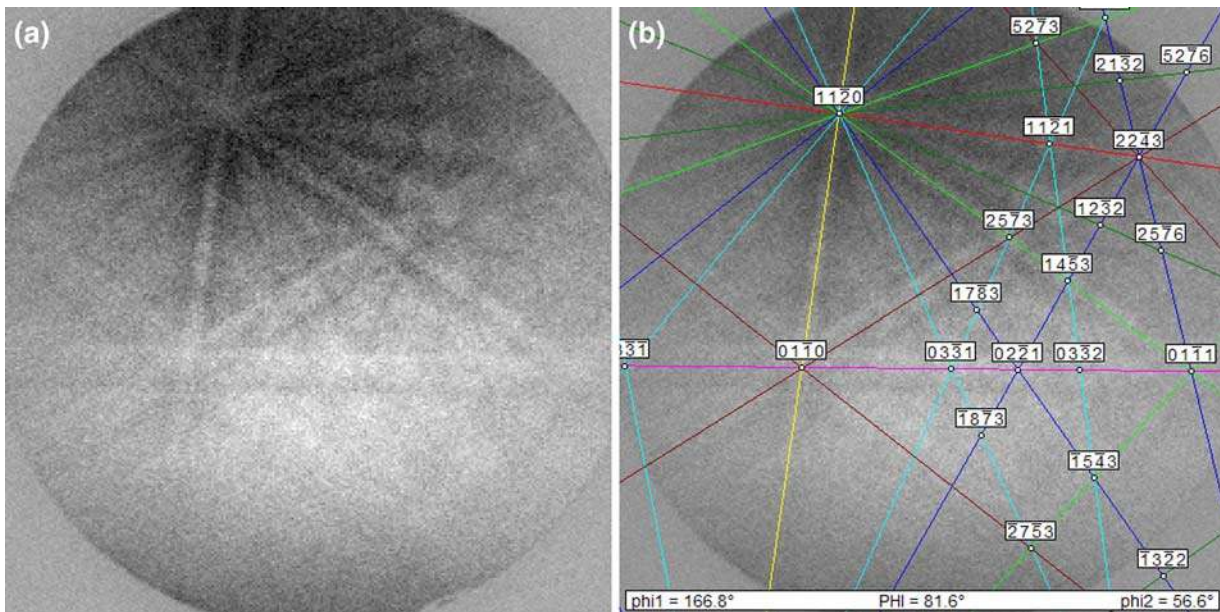

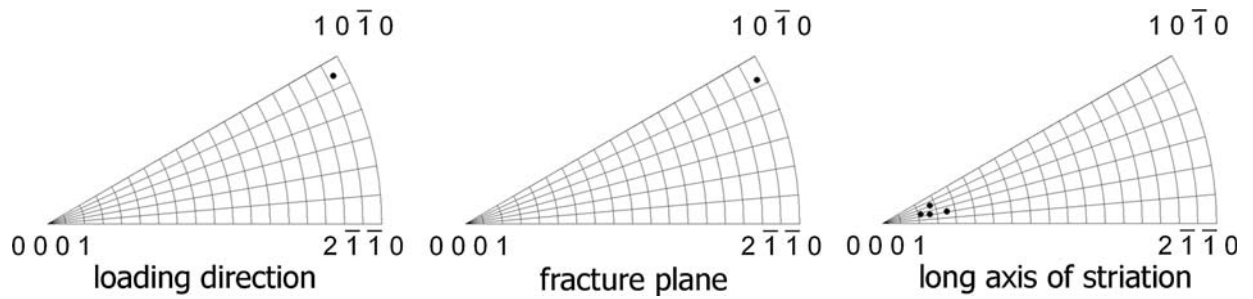Fig. 16—As-collected and indexed EBSD pattern obtained from electropolished region in Fig. 15.

Fig. 17—Equal-angle inverse pole figures identifying crystallographic orientation of the colony containing striations shown in Fig. 15 with respect to loading axis, fracture plane normal, and several vectors along the long axes of the striations.
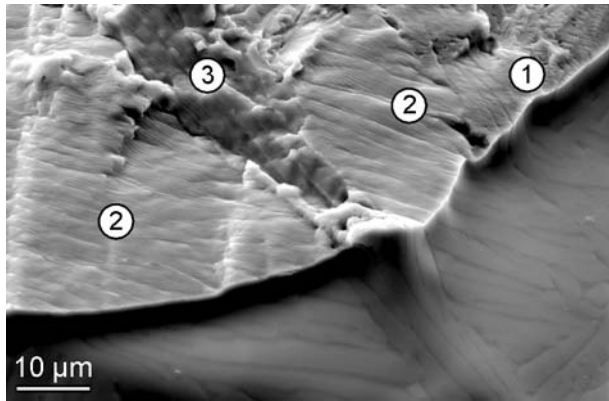

Fig. 18—Fracture surface and underlying microstructure at the intersection of two α colonies.

ribs run approximately parallel with the long axis of the striations; however, this is not sufficient to relate the orientation to the fracture topography. For this purpose, EBSD patterns were acquired from several locations close to the interface of the fracture surface and the electropolished area. The large colony size ensured that the orientation measured near the interface was the same as that beneath the striations. It is noted that this method requires careful interpretation when used on microstructures with shorter length scales. An example of an EBSD pattern collected from the electropolished surface is shown in Figure 16. The pattern was acquired with an acquisition time of 0.03 seconds using a SEM with a tungsten filament source, and the pattern was easily indexed by the automated software. The average fracture plane normal was determined from an area covering over 40 striations to be approximately 13 deg from the loading direction and, with respect to the α-phase lattice (Figure 17), the plane of fracture was calculated to be nearly parallel to one of the $\{10\bar{1}0\}$ planes. This suggests that the crack path through the colony is that which results in the local mode I force acting on the crack tip resolving equal shear stress on two prismatic slip systems. This observation is consistent with Bowen's analysis of the fatigue fracture surfaces of crack propagation specimens made from highly textured Ti-6Al-4V plate. Continuous, regularly spaced striations were formed in specimens in which the grains were oriented for $\{10\bar{1}0\}\langle a\rangle$-type slip, while crack

growth directions were primarily along the $\langle a \rangle$ direction not contained in the active prism slip planes. The long axis of the striations was approximately 15 deg from $[0001]_\alpha$; however, there was increased scatter for this measurement due to the inconsistent height and shape of the fatigue striations. This is evidenced by multiple points on the inverse pole figure in Figure 17 that correspond to measurements made on different individual striations.

Depending on the duration of the electropolishing, a sharp ledge such as that shown in Figure 18 can be created between the fracture surface and the underlying microstructure. This ledge can be relatively quickly removed by FIB milling to reveal the microstructure directly beneath the fracture surface. Using this technique, we have analyzed colonies that have fractured by striation growth as well as a ductile tearing mechanism. The microstructure revealed by FIB milling was investigated with EBSD (Figure 19). One unique β and three unique α orientations were measured on the FIB-milled surface and are shown on discrete equal-angle pole figures in Figure 20. The colonies with orientations designated as 2 and 3 contained classical, regularly spaced fatigue striations. Only a small area of colony 1 was exposed to the FIB-milled surface and the corresponding fracture surface contained faint and discontinuous striation growth. The trace of the long axis of the fatigue striations were again nearly coincident with the 0001 poles in each respective colony (not shown), which is consistent with the site analyzed earlier. The normal to the fracture plane of colony 2 was 13 deg from the loading direction, while the normal of colony 3 had a larger angle of 34.5 deg. After accounting for these orientations, the fracture plane of colony 3 was found to lie near $\{10\bar{1}0\}$, while in contrast, fracture occurred near the $\{11\bar{2}0\}$ plane in colony 2. In both cases, the normal to the macroscopic plane of fracture (which is coincident with the local mode I component acting on the crack tip) resolved equal shear stress on two of the $\{10\bar{1}0\}\langle a\rangle$ slip systems.

A review of the pole figures (Figure 20) shows that there is a significant rotation of the $10\bar{1}0$ and $11\bar{2}0$ poles about the $[0001]_\alpha$ axis, especially in colonies 2 and 3. Based on a substantial number of EBSD observations by the present authors, orientation gradients of this nature are not present in the as-cast and hot isostatically pressed condition. Furthermore, the FIB-milled surface
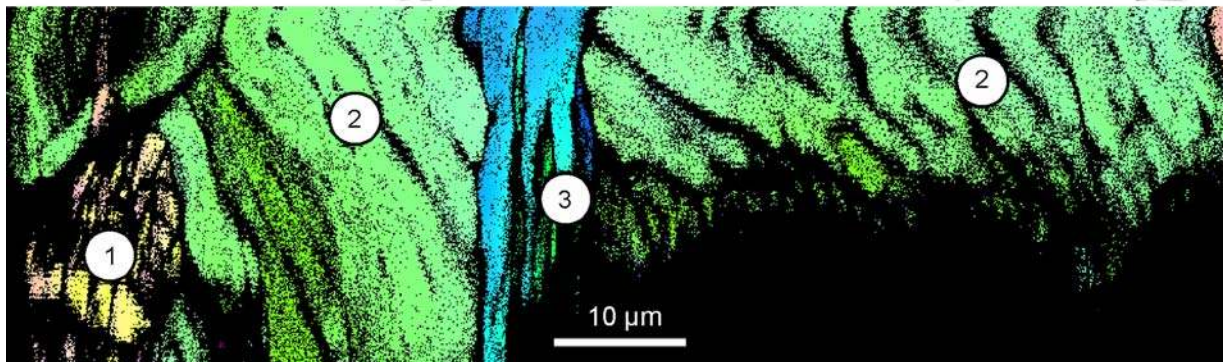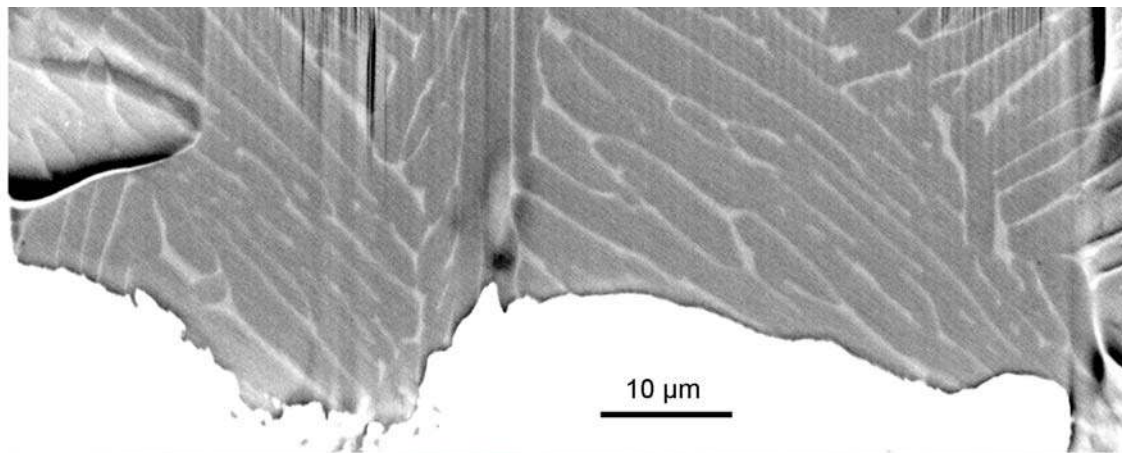
Fig. 19—Backscattered electron micrograph and corresponding orientation map of microstructure beneath fatigue striations shown in Fig. 18.
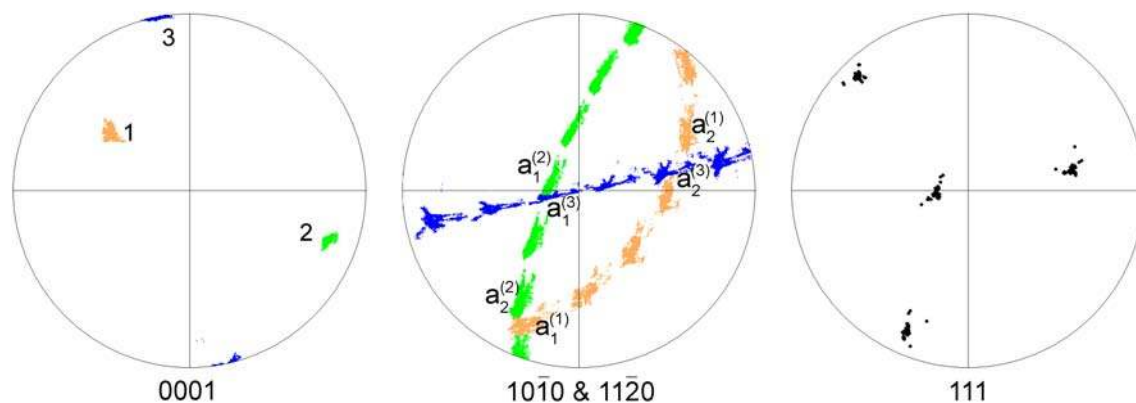

Fig. 20—Discrete equal-angle pole figures showing lattice rotations about the [0001] axis in α phase. The 111 poles of β phase also show evidence of rotation, particularly near the intersection of the $\langle a_1 \rangle$ directions in colonies 2 and 3.

directly borders the fracture surface and so the exposed microstructure must be within the cyclic crack tip plastic zone. Thus, it is probable that the lattice rotations are the result of strain accommodation within the plastic zone. To verify this, orientation data were collected from metallographic sections prepared transverse to the macroscopic fracture plane of several other specimens. Lattice rotations about [0001] were consistently observed in colonies through which cracks advanced by striation growth. Because dislocations are inherently simple shears,[57] there is a net lattice rotation each time dislocation glide occurs. According to crystal plasticity theory,[57] the fact that the rotations occur about the [0001] axis is indicative that strain was accommodated by prismatic $\langle a \rangle$ slip.

As a comparison, colonies oriented with c-axes near the loading axis fail by a different fracture mode and the fracture topography resembles that observed in monotonic loading. An example illustrating the orientation dependence of the fracture topography is shown in Figure 21. The area is shown in the electropolished condition; however, FIB milling followed by EBSD analysis similar to that described earlier were performed in order to collect the orientations shown on the pole
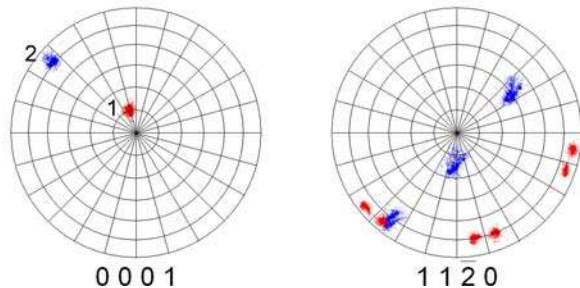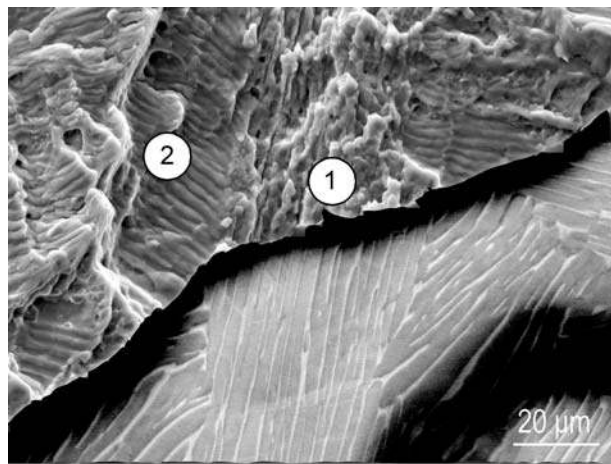
Fig. 21—Fracture surface and underlying microstructure near a colony boundary as well as orientations determined after FIB milling. Loading direction is perpendicular to the plane of the projection.

figures. It is noted that after FIB milling, an additional colony orientation was revealed that shared a common basal plane with colony 1, but this colony was subsurface and did not directly influence fracture topography. The fracture surface of colony 2 is characterized by extensive striation growth, while that of colony 1 has dimpled features corresponding to the α phase with some evidence of cracking along the α/β interface. Based on the locations of the 0001 and $11\bar{2}0$ poles with respect to the loading direction, it can be deduced that colony 2 is suitably oriented for prismatic $\langle a \rangle$ slip, while colony 1 has a high normal stress on the basal plane and low resolved shear stress on all $\langle a \rangle$ slip systems. It is also noted that lattice rotations about [0001] are again evident within the crack tip plastic zone beneath the striations in colony 2, but no rotations are present in colony 1, which did not fail by striation growth. Bowen[39] has speculated that the crack front grows continuously through grains oriented for $\langle a \rangle$ slip, while the other grains are torn as if they were being fractured during a monotonic tension test in the wake of the crack front. The fracture topography of colony 1 is consistent with this in the sense that there are no features that are clearly associated with cyclic fatigue crack propagation.

V. FURTHER DISCUSSION

The use of fractography to study crack initiation relies entirely on the ability of the investigator to distinguish between the initiation and propagation facets. In

general, the facet topography can be used to make this distinction. With increasing distance from the initiation site, the facet surfaces become increasingly rough. This point is evident by comparing the surface roughness of the propagation facet shown in Figure 3(d) with the initiation facet shown in Figure 3(b). The former has extensive surface roughness and there is also evidence of α/β interface cracking. While this is an extreme example, more subtle changes can also be observed between the initiation and propagation facets in Figures 3(b) and (c).

While the crack initiation facets in both specimens bordered the free surface of the sample, crack initiation was clearly not due to a classical slip band intrusion/extrusion mechanism.[31] This was evidenced by the fact that the $\langle a \rangle$ directions, which were parallel to the steps in the facet plane, did not intersect the free surface of the sample. Thus, the active slip system could not have made a surface intrusion/extrusion. The presence of steps on facet surfaces is potentially significant because they are most commonly observed on initiation facets as opposed to propagation facets. For example, similar markings are not observed on the propagation facet shown in Figure 4 and they are distinctly different than the markings on the facet in Figure 3(d). Furthermore, the steps are generally found on facets that are inclined to the loading axis such that there is substantial resolved shear stress on at least one of the basal slip systems. These steps are similar to river markings[32] in that they are indicative of the local crack propagation direction. Thus, it is reasonable to assume that the slip direction parallel to the steps on the facet is the slip system that was active prior to crack initiation. In specimens 1 and 2, the steps were found to be parallel to the $\langle a_1 \rangle$ and $\langle a_2 \rangle$ slip systems, respectively, both of which had the highest resolved shear stress (highest Schmid factor) among the three basal slip systems in their host colonies. The debit in fatigue life for specimen 1 may be related to the fact that an easy basal slip system was active, as opposed to a difficult basal slip system being operative in specimen 2. Other factors, including the local microstructure surrounding the initiation sites and the size of each facet, are also important to the total fatigue life, although it is not possible to determine the relative contribution from each in the present study. It has been shown that single colonies oriented for deformation by $\langle a_2 \rangle$ basal slip have higher yield strength than those oriented for $\langle a_1 \rangle$ basal slip.[18,23] In general, high-cycle fatigue strength scales well with macroscopic yield strength in $\alpha + \beta$ titanium alloys,[58–60] and perhaps this trend also holds for the single-colony/single-crystal level as well. The arrangement of dislocations on the basal slip plane in colonies oriented for $\langle a_2 \rangle$ slip provides insight into the possible mechanism for delaying fatigue crack initiation. The TEM observations by Savage *et al.*[18,23] have shown that dislocation pileups with $\langle a_1 \rangle$- and $\langle a_3 \rangle$-type Burgers vectors are present on the entrance and exit sides of the α/β interfaces of colonies oriented for $\langle a_2 \rangle$ slip. In the case of specimen 2, the $\langle a_1 \rangle$ and $\langle a_3 \rangle$ basal slip systems had low resolved shear stress and thus were not readily mobile. Consequently, the residual interface dislocations are a barrier to subsequent dislocation motion, which could delay crack initiation. In contrast, Savage

et al.[18,23,24] did not observe residual interface dislocations near the α/β interfaces in colonies oriented for ⟨a₁⟩ slip and basal slip transferred easily across the colony. This results in essentially no work hardening and allows dislocations to glide through the colony and concentrate more easily at the grain boundary in colonies in which ⟨a₁⟩ slip is active. Experimental observations have shown that this is where cracks tend to initiate.[13,14,42,59,60] Of particular interest are the experiments conducted by Baxter *et al.*[42] The authors performed four-point-bend fatigue tests on the near-α alloy IMI 834, which accumulates fatigue damage by mechanisms similar to the alloy presently studied. The authors observed fatigue crack initiation at grain boundaries that were below the surfaces of the samples, which were presumed to be stress free due to the electropolishing procedure used to prepare them. In the current investigation, the fractographic investigations suggested crack initiation at boundaries and, furthermore, the EBSD analysis described earlier has found that cracks tend to initiate at boundaries that are crystallographically suited for slip transfer. Whether or not these cracks continue to grow after initiation depends on details of the local microstructure. In passing, although not directly related to the present study due to the difference in crystal symmetries, it is worth mentioning that microcrack initiation in Ti-Al alloys has been observed at grain boundaries that are suited for slip transfer during monotonic loading[48–51] in Ti-Al alloys. In these studies, a statistically significant number of cracked and intact boundaries were analyzed using a combination of crystallographic and geometric criteria to identify those that were prone to microcrack nucleation. These studies motivated the crystallographic analysis presented earlier and support the concept of crack initiation from crystallographic interfaces. It is noted that the geometric criteria were not employed, due to the limited number of misorientations possible between adjacent colonies inherited from the same prior β grain.

With regard to the small cracks revealed by FIB milling, the similarity among the α/α colony boundaries that tended to initiate cracks is striking. All three submerged cracks revealed by FIB milling were observed to form on basal planes that were parallel to a first-order pyramidal plane in an adjacent colony. Thus, a phenomenological mechanism for high-cycle fatigue crack initiation in Burgers-related colony microstructures is proposed and outlined in Figure 22. The β ribs have been omitted from the image to improve clarity and because they would assume a different orientation depending on which basal slip system was active. At a relatively low level of applied stress, only the most suitably oriented slip systems will be activated, with basal and prism slip systems being preferred due to the lower CRSS for slip.[53] The levels of applied stress that produce failures at greater than 10^6 cycles are generally insufficient to activate ⟨c + a⟩ slip and so a dislocation pileup begins to form at an α/α colony boundary. As dislocations enter the pileup, the stress at the head of the pileup increases until it is sufficient to transfer a dislocation through the boundary with its neighbor that
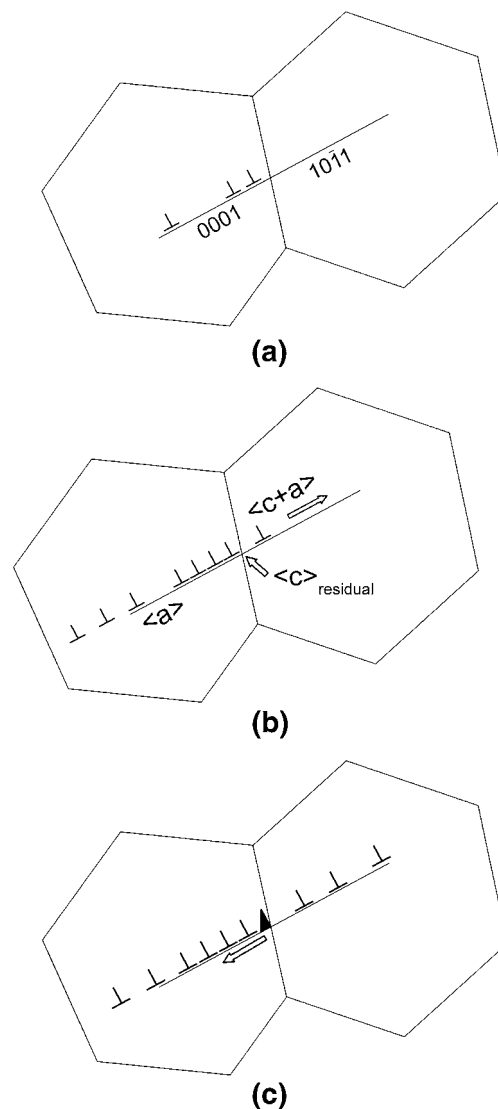

Fig. 22—Schematic for phenomenological model for fatigue crack initiation in Burgers-related colony microstructures: (*a*) a dislocation pileup is formed at grain boundary until a sufficient stress is reached to (*b*) transmit a dislocation through grain boundary, leaving a residual boundary dislocation with a [0001] Burgers vector. Once a sufficient number of dislocation passes through the boundary, a crack is formed that propagates back along the slip band on basal plane.

has a coplanar $\{10\bar{1}1\}\langle11\bar{2}3\rangle$ slip system. This results in the formation of a residual [0001] boundary dislocation. The pileup and transmission process repeats until a sufficient number of boundary dislocations are formed, which acts as a crack nucleus. The crack then propagates back along the slip band on the (0001) plane. Small crack propagation along the basal slip band is preferred over the pyramidal slip plane due to its higher residual dislocation content (higher accumulated damage) and its lower cohesive energy[61] than the adjacent first-order pyramidal system.

It is worth mentioning that multicolony facets have been observed at the catastrophic initiation sites during the present study and also in the literature.[12–14,28,29] There is, however, no experimental evidence in the

present study or in the literature that suggests that cracks initiate at the colony boundaries of the variants related by a 10.5-deg rotation about [0001]. This possibility can be eliminated with fractography by inspecting faceted growth markings that do not lead back to the 10.5 deg about [0001] boundary.[14] Another explanation for the presence of this specific pair of variants at many crack initiation site is that there is a substantial reduction in small crack growth resistance at these low-angle boundaries. High-angle colony boundaries are an effective barrier to small crack growth;[59,60] however, when small cracks encounter a neighboring colony with a common basal plane, crack propagation proceeds with little resistance.[12] Consider the hypothetical situation in which two cracks nucleate at two different locations in the microstructure on the same load cycle. The colonies are both the same size and have an available basal slip length d. The crack grows incrementally with each additional load cycle[12] until it reaches the next colony boundary. The crack in the first colony is arrested at this boundary because there is no closely oriented slip plane with sufficient dislocation debris or low enough cohesive energy to continue advancing by faceted growth. Additionally, the current crack length (d) is sufficiently small that ΔK at the crack tip is not large enough to advance the small crack by conventional striation growth mechanisms. The crack in the second colony, however, has a neighbor with a common basal plane that also has a basal slip length of d. The crack continues to propagate over the colony boundary with little resistance until an effective crack length of $2d$ is obtained. The driving force for further crack propagation increases with ΔK, which increases with increasing crack length, so multicolony facets are already in a more favorable position to become the catastrophic initiation site due to the larger stress intensities at the crack tip. It is acknowledged that fracture mechanics is generally not appropriate to discuss small crack behavior, however, due to the large colony size of the cast and hot isostatically pressed material utilized in this study, a crack that is only one or two colonies can be greater than a millimeter in some cases and, thus, there will be a substantial stress intensity at the crack tip. Thus, one can use this qualitative argument to understand the difference in continued crack propagation in single *vs* multicolony facets in the alloy under investigation. On the other hand, when the colony (or grain) size is much smaller, whether or not small cracks continue to grow depends primarily on the local microstructure,[62] including crystallographic orientation with respect to the applied loading and, perhaps more important, the local neighbor-to-neighbor misorientation.

VI. SUMMARY AND CONCLUSIONS

The complete and thorough characterization of faceted crack initiation sites requires the following two pieces of information: (1) the spatial orientation of the facet plane and (2) the crystallographic plane exposed to the facet surface. We have shown two methods for revealing the microstructure beneath fracture surfaces that utilize electropolishing, the FIB, or both. The FIB-based method is significantly less destructive and has much better spatial accuracy. Crystallographic orientations were determined by collecting EBSD patterns from the FIB-milled surfaces or from the electropolished regions. The lattice orientation was linked to the physical features on the fracture surface through the use of quantitative tilt fractography. These methods permitted the orientation of the β phase to be considered for the first time as it relates to fatigue crack initiation and growth in fully lamellar titanium alloys. The EBSD pattern quality improved significantly on the ion-milled surface after a final low-energy raster mill at 5 kV. The following conclusions regarding the relationship between microstructure and crystallography in Ti-6Al-4V were reached.

1. Two sets of distinct linear markings were observed on the faceted fatigue crack initiation sites. One set was found to be parallel to one of the $\langle a \rangle$ directions in the basal plane, while the other was associated with the α/β interface. The precise basal $\langle a \rangle$ slip system was identified using the crystallographic and geometric relationships imposed by the Burgers orientation relationship.
2. Microstructural and EBSD analysis of three small cracks revealed by FIB milling suggested that all initiated at colony boundaries that were favorably oriented for slip transfer from the $(0001)\langle 11\bar{2}0 \rangle$ slip system to the $\{10\bar{1}1\}\langle 11\bar{2}3 \rangle$ slip system in the adjacent grain. A phenomenological mechanism was proposed in which this type of slip transfer results in the formation of residual [0001] boundary dislocations and eventual crack nucleation and propagation along the basal plane.
3. The fatigue life of a specimen in which the catastrophic crack initiated as a result of $\langle a_1 \rangle$ slip was significantly shorter than another that initiated due to $\langle a_2 \rangle$ slip. This observation was rationalized on the basis of the arrangement of dislocations on the basal plane for each type of slip system; however, the difference in size of the two facets and the orientation of the basal planes of nearby colonies cannot be discounted as contributors to the difference in fatigue life.
4. The long axis of fatigue striations were found to be nearly parallel to the c-axis of the hcp unit cell and formed readily in grains oriented for $\{10\bar{1}0\}\langle a \rangle$ slip. The local mode I component acting on the crack tip can likely be used to predict the growth direction through a particular colony; however, more detailed analyses are required to confirm this.
5. Lattice rotations about the [0001] axis were observed in colonies in which the crack front advanced by striation growth, presumably to accommodate strain within the cyclic crack tip plastic zone.

REFERENCES

1. D.C. Slavik, J.A. Wert, and R.P. Gangloff: *J. Mater. Res.*, 1993, vol. 8 (10), pp. 2482–91.
2. V. Sinha, M.J. Mills, and J.C. Williams: *Metall. Mater. Trans. A*, 2006, vol. 37A, pp. 2015–26.
3. V. Sinha, M.J. Mills, and J.C. Williams: *J. Mater. Sci.*, 2007, vol. 42, pp. 8334–41.
4. Y.J. Ro, S.R. Agnew, and R.P. Gangloff: *Scripta Mater.*, 2005, vol. 52, pp. 531–36.
5. P.A. Davies and V. Randle: *J. Microsc.*, 2001, vol. 204 (1), pp. 29–38.
6. C. Sarrazin, R. Chiron, S. Lesterlin, and J. Petit: *Fatigue Fract. Eng. Mater. Struct.*, 1994, vol. 17 (12), pp. 1383–89.
7. M.R. Bache, W.J. Evans, and H.M. Davies: *J. Mater. Sci.*, 1997, vol. 32, pp. 3435–42.
8. E. Uta, N. Gey, P. Bocher, M. Humbert, and J. Gilgert: *J. Microsc.*, 2009, vol. 233 (3), pp. 451–59.
9. V. Sinha, J.W. Spowart, M.J. Mills, and J.C. Williams: *Metall. Mater. Trans. A*, 2006, vol. 37A, pp. 1507–18.
10. M.R. Bache, W.J. Evans, V. Randle, and R.J. Wilson: *Mater. Sci. Eng., A*, 1998, vol. 257, pp. 139–44.
11. F. Bridier, P. Villechaise, and J. Mendez: *Acta Mater.*, 2008, vol. 56, pp. 3951–62.
12. A.L. Pilchak, A. Bhattacharjee, A.H. Rosenberger, and J.C. Williams: *Int. J. Fatigue*, 2009, vol. 31, pp. 989–94.
13. A.L. Pilchak, A. Bhattacharjee, R.E.A. Williams, and J.C. Williams: *Proc. 12th Int. Conf. on Fracture (CD Proc.)*, Ottawa, ON, Canada, 2009.
14. A.L. Pilchak: Doctoral Dissertation, The Ohio State University, Columbus, OH, 2009.
15. C.C. Wojcik, K.S. Chan, and D.A. Koss: *Acta Metall.*, 1988, vol. 36 (5), pp. 1261–70.
16. K.S. Chan, C.C. Wojcik, and D.A. Koss: *Metall. Trans. A*, 1981, vol. 12A, pp. 1899–1907.
17. S. Suri, G.B. Viswanathan, T. Neeraj, D.-H. Hou, and M.J. Mills: *Acta Mater.*, 1999, vol. 47 (3), pp. 1019–34.
18. M.F. Savage, J. Tatalovich, and M.J. Mills: *Philos. Mag.*, 2004, vol. 84 (11), pp. 1127–54.
19. K.S. Chan: *Metall. Mater. Trans. A*, 2004, vol. 35A, pp. 3409–22.
20. G. Themelis, S. Chikwembani, and J. Weerman: *Mater. Charact.*, 1990, vol. 24, pp. 27–40.
21. W.G. Burgers: *Physica*, 1934, vol. 1, pp. 561–86.
22. M.J. Mills, D.H. Hou, S. Suri, and G.B Viswanathan: *Boundaries and Interfaces in Materials*, TMS, Warrendale, PA, 1998, pp. 295–301.
23. M.F. Savage: Doctoral Dissertation, The Ohio State University, Columbus, OH, 2000.
24. M.F. Savage, J. Tatalovich, M. Zupan, K.J. Hemker, and M.J. Mills: *Mater. Sci. Eng., A*, 2001, vols. 319–321, pp. 398–403.
25. S.C. Wang, M. Aindow, and M.J. Starink: *Acta Mater.*, 2003, vol. 51, pp. 2485–2503.
26. D. Bhattacharyya, G.B. Viswanathan, R. Denkenberger, D. Furrer, and H.L. Fraser: *Acta Mater.*, 2003, vol. 51, pp. 4679–91.
27. D. Bhattacharyya: Doctoral Dissertation, The Ohio State University, Columbus, OH, 2004.
28. D. Eylon: *J. Mater. Sci.*, 1979, vol. 14, pp. 1914–22.
29. D. Eylon: *Trans. TMS-AIME*, 1979, vol. 10 (3), pp. 311–17.
30. A.L. Pilchak and J.C. Williams: *Metall. Mater. Trans. A*, 2009, vol. 40A, pp. 2603–15.
31. S. Suresh: *Fatigue of Materials*, 2nd ed., Cambridge University Press, New York, NY, 1998.
32. A. Barna, B. Pecz, and M. Menyhard: *Ultramicroscopy*, 1998, vol. 70, pp. 161–71.
33. J.P McCaffrey, M.W. Phaneuf, and L.D. Madsen: *Ultramicroscopy*, 2001, vol. 87, pp. 97–104.
34. K. Nordlund, M. Ghaly, R.S. Averback, M. Caturla, T. Diaz de la Rubia, and J. Taurus: *Phys. Rev. B*, 1998, vol. 57 (13), pp. 7556–70.
35. C.D. Beachem and R.M.N. Pelloux: *Fracture Toughness Testing and Its Applications*, ASTM STP 381, ASTM, Philadelphia, PA, 1965, pp. 210–45.
36. U. Dahmen: *Acta Metall.*, 1982, vol. 30, pp. 63–73.
37. H.-J. Bunge: *Texture Analysis in Materials Science: Mathematical Methods*, Butterworth & Co., Berlin, 1982, pp. 55–118.
38. J.F. Nye: *Physical Properties of Crystals: Their Representation by Tensors and Matrices*, Oxford University Press, New York, NY, 1985, pp. 276–83.
39. A.W. Bowen: *Acta Metall.*, 1975, vol. 23 (11), pp. 1401–09.
40. M.G. Glavicic, P.A. Kobryn, T.R. Bieler, and S.L. Semiatin: *Mater. Sci. Eng., A*, 2003, vol. 346, pp. 50–59.
41. M.G. Glavicic, P.A. Kobryn, T.R. Bieler, and S.L. Semiatin: *Mater. Sci. Eng., A*, 2003, vol. 351, pp. 258–64.
42. G.J. Baxter, W.M. Rainforth, and L. Grabowski: *Acta Mater.*, 1996, vol. 44 (9), pp. 3453–63.
43. W.J. Evans and M.R. Bache: *Int. J. Fatigue*, 1994, vol. 16 (7), pp. 443–52.
44. J.V. Bernier, J.-S. Park, A.L. Pilchak, M.G. Glavicic, and M.P. Miller: *Metall. Mater. Trans. A*, 2008, vol. 39A, pp. 3120–33.
45. *Electron Backscatter Diffraction in Materials Science*, A.J. Schwartz, M. Kumar, and B.L. Adams, eds., Kluwer Academic/Plenum Publishers, New York, NY, 2000, p. 9.
46. J. Luster and M.A. Morris: *Metall. Mater. Trans. A*, 1995, vol. 26A, pp. 1745–56.
47. W.A.T. Clark, R.H. Wagoner, Z.Y. Shen, T.C. Lee, I.M. Robertson, and H.K. Birnbaum: *Scripta Metall. Mater.*, 1992, vol. 26, pp. 203–06.
48. B.A. Simkin, M.A. Crimp, and T.R. Bieler: *Scripta Mater.*, 2003, vol. 49, pp. 149–54.
49. T.R. Bieler, A. Fallahi, B.C. Ng, D. Kumar, M.A. Crimp, B.A. Simkin, A. Zamiri, F. Pourboghrat, and D.E. Mason: *Intermetallics*, 2005, vol. 13, pp. 979–84.
50. A. Fallahi, D.E. Mason, D. Kumar, T.R. Bieler, and M.A. Crimp: *Mater. Sci. Eng., A*, 2006, vol. 432, pp. 281–91.
51. D. Kumar, T.R. Bieler, P. Eisenlohr, D.E. Mason, M.A. Crimp, F. Roters, and D. Raabe: *J. Eng. Mater. Technol.*, 2008, vol. 130, pp. 021012-1–021012-12.
52. T.R. Bieler and S.L. Semiatin: *Int. J. Plast.*, 2002, vol. 18, pp. 1165–89.
53. J.C. Williams, R.G. Baggerly, and N.E. Paton: *Metall. Mater. Trans. A*, 2002, vol. 33A, pp. 837–50.
54. M.J. Blackburn and J.C. Williams: *Trans. ASM*, 1969, vol. 62, pp. 398–409.
55. A.H. Cottrell: *Trans. AIME*, 1958, vol. 212, pp. 192–203.
56. J.C. Chesnutt and R.A. Spurling: *Metall. Trans. A*, 1977, vol. 8A, pp. 216–18.
57. U.F. Kocks, C.N. Tomé, and H.-R. Wenk: *Texture and Anisotropy: Preferred Orientations in Polycrystals and Their Effect on Materials Properties*, Cambridge University Press, New York, NY, 1998, pp. 282–325.
58. J.C. Chesnutt, A.W. Thompson, and J.C. Williams: *Influence of Metallurgical Factors on the Fatigue Crack Growth Rate in Alpha-Beta Titanium Alloys*, Final Technical Report AFML-TR-78-68, Air Materials Laboratory, Wright Patterson, 1978, pp. 1–269.
59. G. Lütjering: *Mater. Sci. Eng., A*, 1998, vol. 243, pp. 32–35.
60. G. Lütjering and J.C. Williams: *Titanium*, Springer-Verlag, New York, NY, 2003, pp. 177–232.
61. S. Erdin, Y. Lin, and J.W. Halley: *Phys. Rev. B*, 2005, vol. 72, pp. 1–6.
62. C. Szczepanski: Doctoral Dissertation, University of Michigan, Ann Arbor, MI, 2008.